

Numerical Simulation of Deformation and Failure Behavior of Geosynthetic Reinforced Soil Bridge Abutments

Yewei Zheng, A.M.ASCE¹; Patrick J. Fox, F.ASCE²; and John S. McCartney, M.ASCE³

Abstract: This paper presents a numerical investigation of the deformation and failure behavior of geosynthetic reinforced soil (GRS) bridge abutments. The backfill soil was characterized using a nonlinear elasto-plastic constitutive model that incorporates a hyperbolic stress-strain relationship with strain softening behavior and the Mohr-Coulomb failure criterion. The geogrid reinforcement was characterized using a hyperbolic load-strain-time model. The abutments were numerically constructed in stages, including soil compaction effects, and then monotonically loaded in stages to failure. Simulation results indicate that a nonlinear reinforcement model is needed to characterize deformation behavior for high applied stress conditions. A parametric study was conducted to investigate the effects of reinforcement, backfill soil, and abutment geometry on abutment deformations and failure. Results indicate that reinforcement spacing, reinforcement stiffness, backfill soil friction angle, and abutment height are the most significant parameters. The shape of the failure surface is controlled by abutment geometry and can be approximated as bilinear.

Keywords: Geosynthetic reinforced soil; Bridge abutment; Numerical simulation; Service limit; Strength limit; Failure mechanism.

¹ Postdoctoral Research Scholar, Department of Structural Engineering, University of California, San Diego, La Jolla, CA 92093-0085 USA (corresponding author). Email: y7zheng@ucsd.edu

² Shaw Professor and Head, Department of Civil and Environmental Engineering, Pennsylvania State University, University Park, PA 16802 USA. Email: pjfox@engr.psu.edu

³ Associate Professor, Department of Structural Engineering, University of California, San Diego, La Jolla, CA 92093-0085 USA. Email: mccartney@ucsd.edu

22 Introduction

23 Geosynthetic reinforced soil (GRS) bridge abutments are becoming widely used in
24 transportation infrastructure and provide many advantages over traditional pile-supported
25 designs, including lower cost, faster and easier construction, and smoother transition between the
26 bridge and approach roadway. Several case histories for in-service GRS bridge abutments have
27 been reported and show good field performance (Won et al. 1996; Wu et al. 2001; Abu-Hejleh et
28 al. 2002; Adams et al. 2011a; Saghebfar et al. 2017). Numerical studies also have been
29 conducted for GRS bridge abutments under service load conditions (Helwany et al. 2003, 2007;
30 Zheng et al. 2014, 2015; Ambauen et al. 2015; Zheng and Fox 2016a, 2017; Ardah et al. 2017).
31 These studies considered perfectly plastic soil and linearly elastic geosynthetic reinforcement
32 and indicate relatively small lateral facing displacements and vertical strains. Numerical
33 modeling work on the deformation behavior and bearing capacity of GRS bridge abutments,
34 associated with large deformations up to failure, is more limited and also has assumed perfectly
35 plastic soil and linearly elastic geosynthetic reinforcement (Wu et al. 2006a). Based on other
36 related research findings (e.g., Walters et al. 2002; Hatami and Bathurst 2006; Liu and Ling 2012;
37 Yang et al. 2012; Zheng and Fox 2016b), strain softening of the backfill soil and nonlinear
38 response of the geosynthetic reinforcement may be important for high applied stress conditions.
39 An investigation considering these effects, including failure behavior, would represent a useful
40 contribution to the literature.

41 This paper presents a numerical investigation of the deformation and failure behavior of
42 GRS bridge abutments. Simulations were performed to identify the importance of strain
43 softening soil and nonlinear reinforcement behavior for a baseline case, and a parametric study
44 was conducted to investigate the effects of reinforcement, backfill soil, and abutment geometry

45 on abutment deformations and failure. Results from this study provide insights with regard to
46 the design of GRS bridge abutments for various loading conditions.

47

48 **Background**

49 Deformations, such as lateral facing displacements and vertical compressions, are
50 important considerations in the design of GRS bridge abutments for the service limit condition,
51 whereas bearing capacity is an important consideration for the strength limit condition. The
52 Federal Highway Administration (FHWA) provides analytical and empirical design methods for
53 both conditions (Adams et al. 2011a, 2011b). The FHWA analytical method calculates ultimate
54 bearing capacity based on the soil-geosynthetic composite load bearing capacity, which accounts
55 for the maximum aggregate size and friction angle of the backfill soil and the spacing and
56 ultimate tensile strength of the geosynthetic reinforcement (Wu and Pham 2013; Wu et al. 2013).
57 The allowable vertical stress for the service limit is then taken as 10% of the ultimate bearing
58 capacity (Nicks et al. 2013, 2016). The FHWA empirical method is based on a vertical stress-
59 strain relationship that is measured from performance tests (i.e., GRS mini-pier loading tests)
60 conducted using project-specific soil and geosynthetic materials (Adams et al. 2011a, 2011b). In
61 this case, the service limit is defined as an applied vertical stress of 200 kPa or the vertical stress
62 at 0.5% vertical strain, and the strength limit is defined as the vertical stress at 5% vertical strain
63 (Berg et al. 2009; Adams et al. 2011a, 2011b; Nicks et al. 2013).

64 Field and laboratory loading tests have been conducted on large-scale GRS piers and
65 abutments and generally indicate satisfactory performance under service loads and relatively
66 high bearing capacity (Adams 1997; Gotteland et al. 1997; Ketchart and Wu 1997; Wu et al.
67 2001, 2006a; Adams et al. 2011b, 2014; Nicks et al. 2013, 2016; Iwamoto et al. 2015). Lee and

68 Wu (2004) reviewed the results of several large-scale loading tests and suggested that bearing
69 capacity can be as high as 900 kPa for closely spaced reinforcement and well-graded, well-
70 compacted backfill soil. Nicks et al. (2013) conducted a series of performance tests on 2 m-high
71 GRS mini-piers and found that reinforcement spacing and tensile strength have the most
72 important effects on ultimate bearing capacity, and that well-graded backfill materials and
73 increasing levels of backfill compaction can increase the stiffness of a GRS mini-pier.

74 Wu et al. (2006a) conducted numerical simulations on the deformation behavior of GRS
75 bridge abutments using a geologic cap model for the backfill soil and a linearly elastic model for
76 the geosynthetic reinforcement, and developed procedures to determine allowable vertical stress
77 considering bridge seat type, reinforcement spacing, and backfill soil properties. Leshchinsky
78 (2014) and Xie and Leshchinsky (2015) performed a series of parametric studies using limit
79 analysis to investigate the optimal reinforcement design and failure mechanism of GRS bridge
80 abutments, and found that reinforcement with closer vertical spacing in the upper section can
81 efficiently increase the ultimate bearing capacity. Results also showed a curved failure surface
82 extending downward from the heel of the bridge seat to the toe of the abutment for a bridge seat
83 setback distance of 1.35 m or less and a compound failure surface for greater setback distances.

84

85 **Numerical Model**

86 The two-dimensional finite difference program *FLAC Version 7.0* (Itasca Consulting
87 Group 2011) was used for the current investigation. Zheng and Fox (2016a) developed a *FLAC*
88 model to simulate the field performance of the Founders/Meadows GRS bridge abutment (Abu-
89 Hejleh et al. 2000, 2001). Simulation results, including lateral facing displacements, bridge seat
90 settlements, lateral and vertical earth pressures, and reinforcement tensile strains and forces,

91 were in good agreement with field measurements at various stages of construction. Using a
92 similar modeling approach, Zheng and Fox (2017) simulated the response of a geosynthetic
93 reinforced soil-integrated bridge system (GRS-IBS) abutment and found good agreement for
94 abutment vertical compression measurements reported by Adams et al. (2011a). Based on these
95 results, Zheng and Fox (2016a, 2017) concluded that this type of numerical model has the
96 capability to simulate the performance of GRS bridge abutments under service load conditions.
97 In the current study, the model has been enhanced by incorporating strain softening behavior for
98 the backfill soil and nonlinear behavior for the geosynthetic reinforcement to simulate the
99 deformation of GRS bridge abutments up to failure conditions. The explicit Lagrangian
100 calculation method and mixed-discretization zoning technique used in *FLAC* are well suited for
101 this purpose, with the ability to characterize plastic deformations and strain localization. *FLAC*
102 is applicable for plane strain conditions, which represents a simplification for these three-
103 dimensional structures.

104

105 **Baseline Case**

106 **Geometry**

107 The finite difference grid and boundary conditions for the GRS bridge abutment baseline
108 case are shown in Fig. 1. The model represents a single-span bridge system with span $L_b = 30$
109 m and symmetrical structures on both ends. Each end structure consists of a lower GRS wall,
110 bridge seat, upper GRS fill, and approach roadway. Only the right-hand side of the bridge
111 system was simulated due to symmetry. The GRS bridge abutment has height $h = 5$ m and 25
112 modular facing blocks with dimensions of 0.3 m (length) \times 0.2 m (height). An L-shaped bridge
113 seat with a section thickness of 0.4 m rests on top of the GRS bridge abutment and has setback

114 distance $a_b = 0.2$ m from the wall facing. The clear distance between the top facing block and
115 bridge beam d_e is equal to the bridge seat thickness (0.4 m). The clearance height for the bridge
116 beam above the foundation soil is 5.4 m, which satisfies the FHWA minimum requirement of 4.9
117 m for interstate highways (Stein and Neuman 2007). The bridge seat has upper surface contact
118 length $L_c = 1.0$ m with the bridge beam and lower surface contact length $L_s = 1.5$ m with the
119 soil. There is a 100 mm-wide vertical expansion joint between the bridge beam and bridge seat.
120 Assuming a ratio of bridge beam span to depth $R_{sd} = L_b / D = 20$, the depth of the bridge beam
121 $D = 1.5$ m. A 1.8 m-high upper GRS fill lies behind the bridge seat and is overlain by a 0.1 m-
122 thick concrete roadway. The reinforcement has uniform length $L_r = 3.5$ m ($0.7h$) and vertical
123 spacing $S_v = 0.2$ m for both the lower GRS wall and upper GRS fill. No secondary (i.e., bearing
124 bed) reinforcement is included under the bridge seat for the baseline case.

125 To minimize the influence of boundary conditions on system response, the foundation
126 soil has a depth of 10 m ($2h$) and the rear boundary is located at a distance of 20 m ($4h$) from
127 the wall facing. Lateral boundaries are fixed in the horizontal direction and are free to move in
128 the vertical direction, whereas the bottom boundary is fixed in both horizontal and vertical
129 directions. Horizontal coordinate x is measured to the right from the back side of the wall
130 facing and vertical coordinate z is measured upward from the top surface of the foundation soil.

131

132 Soils

133 Zheng and Fox (2016a) simulated the static response of the Founders/Meadows GRS
134 bridge abutment using a nonlinear elasto-plastic model with a hyperbolic relationship and a
135 Mohr-Coulomb failure criterion for the backfill soil. In the current investigation, the model is

136 enhanced by incorporating strain softening behavior at larger strain levels to simulate the
 137 response of GRS bridge abutments up to failure conditions. The tangent elastic modulus E_t ,
 138 unloading-reloading modulus E_{ur} , bulk modulus B , and tangent Poisson's ratio ν_t are
 139 expressed as (Duncan et al. 1980):

$$140 \quad E_t = \left[1 - \frac{R_f (1 - \sin \phi') (\sigma'_1 - \sigma'_3)}{2c' \cos \phi' + 2\sigma'_3 \sin \phi'} \right]^2 K p_a \left(\frac{\sigma'_3}{p_a} \right)^n \quad (1)$$

$$141 \quad E_{ur} = K_{ur} p_a \left(\frac{\sigma'_3}{p_a} \right)^n \quad (2)$$

$$142 \quad B = K_b p_a \left(\frac{\sigma'_3}{p_a} \right)^m \quad (3)$$

$$143 \quad \nu_t = \frac{1}{2} - \frac{E_t}{6B} \quad (4)$$

144 where σ'_1 and σ'_3 = major and minor principal effective stresses; ϕ' = friction angle; c' =
 145 cohesion; R_f = failure ratio; K = elastic modulus number; n = elastic modulus exponent; p_a =
 146 atmospheric pressure; K_{ur} = unloading-reloading modulus number; K_b = bulk modulus number;
 147 m = bulk modulus exponent; and ν_t is limited to a range of 0 to 0.49. Eqs. (1-4) were
 148 implemented into *FLAC* using FISH subroutines to update the stress-dependent soil moduli
 149 during the course of each simulation. To account for strain softening behavior, the friction angle
 150 and dilation angle were defined as piece-wise linear functions of incremental plastic shear strain
 151 and calibrated using triaxial test data.

152 Backfill soil properties are based on measurements for a well-graded angular sand with
 153 maximum particle size $d_{max} = 9.5$ mm, which meets the FHWA specifications for GRS bridge
 154 abutments (Berg et al. 2009; Adams et al. 2011b). Consolidated-drained triaxial compression

155 tests were conducted on sand specimens at five levels of effective confining stress. The
156 specimens were compacted at a relative density of 80% with unit weight $\gamma = 17.3 \text{ kN/m}^3$. The
157 tests were numerically simulated and soil parameters were back-calculated from the
158 experimental results. The resulting piece-wise linear relationships between incremental plastic
159 shear strain ε_p , which occurs once the soil reaches the Mohr-Coulomb failure criterion, and the
160 friction angle and dilation angle are shown in Fig. 2. The soil responds with peak values of
161 friction angle and dilation angle of $\phi'_p = 46^\circ$ and $\psi_p = 18^\circ$, respectively, for $\varepsilon_p = 0\%$ to 4%. For
162 $\varepsilon_p = 4\%$ to 15%, the soil experiences post-peak strain softening where both angles decrease
163 linearly. For $\varepsilon_p \geq 15\%$, the soil responds with constant volume (i.e., steady state) friction angle
164 and dilation angle of $\phi'_{cv} = 43^\circ$ and $\psi_{cv} = 0^\circ$, respectively. Using these relationships, a
165 comparison of measured and simulated triaxial test results is shown in Fig. 3. The simulations
166 slightly underestimate the deviator stress at the two lower confining stress levels; however, the
167 nonlinear stress-strain behavior before peak strength and post-peak strain softening are
168 characterized with good accuracy, especially for the higher confining stresses. The simulated
169 response for soil dilation behavior is also in good agreement with the measured data.

170 The foundation soil was specified as dense silty sandy gravel and simulated using a
171 linearly elastic-perfectly plastic model with a Mohr-Coulomb failure criterion. A firm
172 foundation soil was used for all simulations for consistency. A summary of parameters for the
173 backfill soil and foundation soil is provided in Table 1.

174

175 Reinforcement

176 Geogrid reinforcement was included in the numerical model using cable elements rigidly
177 connected to the facing blocks and characterized using the hyperbolic load-strain-time model

178 proposed by Allen and Bathurst (2014a, 2014b). Yu et al. (2016) also used this model and
 179 provided further discussion. Tensile force T is calculated as the product of tensile strain ε and
 180 a strain- and time-dependent secant stiffness J_s as:

$$181 \quad T = J_s \varepsilon \quad (5)$$

182 where

$$183 \quad J_s = \frac{1}{\frac{1}{J_0} + \chi \varepsilon} \quad (6)$$

184 and J_0 = initial tangent stiffness and χ = empirical fitting parameter, with both J_0 and χ
 185 expressed as functions of time t . Tangent stiffness J_t of the reinforcement is calculated as:

$$186 \quad J_t = \frac{1}{J_0 \left(\frac{1}{J_0} + \chi \varepsilon \right)^2} \quad (7)$$

187 and the input parameter for elastic modulus is defined as:

$$188 \quad E_r = J_t / t_r \quad (8)$$

189 where t_r = geogrid thickness (constant).

190 A high density polyethylene (HDPE) uniaxial geogrid was specified for the GRS bridge
 191 abutment, with properties and tensile behavior shown as Geogrid-2 in Fig. 4. The stiffness
 192 parameters are initial stiffness $J_0 = 1054 t^{-0.0697}$ kN/m and $\chi = 0.0359$ m/kN. Yu et al. (2016)
 193 reported that the stiffness values for several HDPE geogrids were not significantly affected by
 194 practical construction times of interest and, for simplicity, can be taken as constant during
 195 construction. Following this procedure, an end-of-construction time $t = 150$ days = 3600 hours
 196 was specified for the current simulations. As such, the tensile behavior for Geogrid-2 is
 197 characterized by $J_0 = 596$ kN/m and shows stiffness decreasing nonlinearly with increasing

198 strain. A summary of parameters for Geogrid-2 is provided in Table 2. Geogrid-1 and Geogrid-
199 3 are discussed later for the parametric study.

200

201 **Structural Components**

202 The concrete facing blocks, bridge seat, and roadway were modeled as linearly elastic
203 materials with unit weight $\gamma = 23.5 \text{ kN/m}^3$, elastic modulus $E = 20 \text{ GPa}$, and Poisson's ratio ν
204 $= 0.2$. The bridge beam was modeled as a solid block ($L_b \times D \times 1$) of linearly elastic material
205 with $E = 20 \text{ GPa}$ and $\nu = 0.2$. The unit weight of the bridge beam γ_b was changed to produce
206 different values of applied vertical stress on the GRS bridge abutment during the loading stage of
207 the numerical simulations. The vertical force per unit width on the GRS bridge abutment is
208 $F_v = L_b D \gamma_b / 2$, and the corresponding average applied vertical stress on the lower surface of the
209 bridge seat is $q_v = F_v / L_s$.

210

211 **Interfaces**

212 Table 3 presents parameters for the various interfaces between soil, geogrid, facing block,
213 bridge seat, and bridge beam. Soil-geogrid interfaces were included with the respective cable
214 elements, whereas specific interface elements were needed to define block-block, soil-block,
215 soil-bridge seat, and bridge beam-bridge seat interfaces. The soil-geogrid interfaces account for
216 shear stiffness k_s , friction angle δ'_i , and adhesion c'_i , whereas the other interfaces account for
217 these parameters and normal stiffness k_n in addition. Soil interface strengths were characterized
218 using a reduction factor RF defined as

$$219 \quad RF = \frac{\tan \delta'_i}{\tan \phi'_p} = \frac{c'_i}{c'} \quad (9)$$

220 Considering the typical embedment of wall facing at the toe of a GRS bridge abutment in the
221 field, a relatively high toe shear stiffness of 40 MPa/m, as suggested by Yu et al. (2016), was
222 selected for the interface between the lowermost facing block and foundation soil. The frictional
223 interface between the bridge beam and bridge seat produces a lateral restraining force on the
224 abutment structure, which can have an important effect on abutment deformations (Zheng and
225 Fox 2016a).

226

227 **Modeling Procedures**

228 For each numerical simulation, the GRS bridge abutment model was constructed in
229 stages and then monotonically loaded in stages to failure. Initially, the foundation soil was
230 placed and resolved to equilibrium under gravitational forces. The GRS bridge abutment was
231 constructed in layers on top of the foundation soil, with each layer consisting of one soil lift, one
232 facing block, and the necessary interfaces. Geogrid reinforcement layers were placed at
233 specified elevations, depending on the simulation. Following Hatami and Bathurst (2006), Guler
234 et al. (2007), Zheng and Fox (2017), and Zheng et al. (2017), a temporary uniform surcharge
235 stress of 8 kPa was applied to the top surface of each soil lift to simulate the effect of compaction
236 and then removed prior to application of the next lift. On removal of the surcharge stress, the
237 soil follows an unloading path with higher stiffness, which is similar to the paths for
238 axisymmetric unloading shown as examples for the simulated stress-strain relationships in Fig.
239 3(a). Reloading follows the same path and, as such, each soil lift has an initially stiffer response
240 during placement of the next lift. Once the GRS bridge abutment was completed, the bridge seat
241 was placed on the abutment, the upper GRS fill was similarly constructed in layers behind the

242 bridge seat, and the approach roadway was placed on the GRS fill. The bridge beam then was
243 placed on the bridge seat with an initial unit weight $\gamma_b = 3.34 \text{ kN/m}^3$, which was chosen to
244 produce an initial average applied vertical stress of $q_v = 50 \text{ kPa}$. During subsequent loading, the
245 unit weight of the bridge beam was increased in stages to produce failure of the abutment. For
246 each construction and loading stage, the numerical model was resolved to equilibrium under
247 gravitational forces. Abutment failure was assumed to occur if *FLAC* could not converge to
248 equilibrium or the abutment reached a vertical strain of 10%.

249 Results from the numerical simulations are assessed at conditions of service limit and
250 strength limit for the GRS bridge abutment. Similar to Nicks et al. (2013, 2016), the service
251 limit is defined according to two criteria. The first criterion is an average applied vertical stress
252 of $q_v = 200 \text{ kPa}$ and the second criterion is an average vertical strain of $\varepsilon_v = 0.5\%$, where ε_v is
253 based on abutment compression defined as the difference between the average downward
254 displacement of the bridge seat and the average downward displacement of the underlying
255 foundation soil. The strength limit is defined as an average vertical strain of $\varepsilon_v = 5\%$ and is
256 based on considerations of ultimate bearing capacity as per FHWA guidelines (Nicks et al. 2013).

257

258 ***PPS and LER Cases***

259 In addition to the baseline case defined by the above modeling conditions and parameters,
260 simulations were also performed for two additional cases to investigate the effects of soil strain
261 softening and nonlinear reinforcement behavior on the deformation response of the GRS bridge
262 abutment. The first additional case assumes perfectly plastic soil (PPS) with constant values of
263 friction angle and dilation angle ($\phi' = 46^\circ$ and $\psi = 18^\circ$) and nonlinear reinforcement (as per the
264 baseline case). The second additional case assumes linearly elastic reinforcement (LER) with

265 constant stiffness equal to the secant stiffness at 5% tensile strain $J_{5\%} = 620$ kN/m, and strain
266 softening soil (as per the baseline case).

267

268 **Simulation Results**

269 Lateral facing displacement profiles for the baseline, PPS, and LER cases and two levels
270 of average applied vertical stress $q_v = 400$ kPa and $q_v = 800$ kPa are presented in Fig. 5(a). At
271 $q_v = 400$ kPa for the baseline case, a maximum lateral displacement of 60.6 mm occurs near the
272 top of the wall at elevation $z = 4.2$ m above the foundation soil. Lateral displacements for the
273 baseline and PPS cases are in close agreement and larger than for the LER case. At $q_v = 800$
274 kPa, lateral displacements increase significantly and the trends are similar. The baseline case
275 yields the largest lateral displacements with a maximum value of 148.4 mm at $z = 4.0$ m.
276 Maximum lateral displacements for the PPS and LER cases are 138.0 mm and 75.0 mm,
277 respectively. Corresponding profiles of maximum tensile force in the geogrid reinforcement are
278 presented in Fig. 5(b). At $q_v = 400$ kPa, the maximum tensile force (13.9 kN/m) occurs at $z =$
279 4.8 m for the baseline case with an associated tensile strain of 4.7%. The factor of safety (FS)
280 against reinforcement rupture is 5.0, based on the ultimate tensile strength $T_{ult} = 70$ kN/m (Table
281 2). For the PPS and LER cases, maximum tensile forces are 13.7 kN/m and 16.1 kN/m, and FS
282 = 5.1 and 4.3, respectively. Maximum tensile forces for the baseline and PPS cases are in close
283 agreement and slightly smaller than for the LER case. At $q_v = 800$ kPa, maximum tensile forces
284 increase significantly and the trends are similar; however, maximum tensile forces for the LER
285 case are much larger than for the baseline and PPS cases near the top of the wall. The maximum
286 tensile force of 21.3 kN/m occurs at $z = 4.6$ m for the baseline case with a corresponding tensile

287 strain of 14.4% and $FS = 3.3$. Maximum tensile forces are 21.0 kN/m and 33.6 kN/m for the
288 PPS and LER cases, respectively, with corresponding values of $FS = 3.3$ and $FS = 2.1$.

289 The results of Fig. 5 show that, at the higher applied vertical stress $q_v = 800$ kPa, lateral
290 displacements and maximum tensile forces are nearly equal for the baseline and PPS cases. This
291 suggests that post-peak strain softening behavior for the soil is not a critical consideration for the
292 conditions simulated. On the other hand, lateral displacements are much lower and maximum
293 tensile forces are much higher for the LER case, which suggests that the geosynthetic
294 constitutive model (i.e., linear vs. nonlinear) has a significant effect. Reinforcement stiffness is
295 constant for the LER case and decreases significantly with increasing strain for the baseline and
296 PPS cases (Fig. 4). As the applied vertical stress on the abutment increases and soil stiffness
297 decreases, the reinforcement picks up a greater fraction of this load for the LER case.

298 Plots of maximum lateral facing displacement, average abutment compression, and
299 corresponding average abutment vertical strain (ε_v) vs. average applied vertical stress (q_v) for
300 the three simulation cases are shown in Fig. 6. In general, the results indicate that the baseline
301 and PPS cases display nonlinear responses, whereas the LER case shows a nearly linear response.
302 On both plots, deformations are essentially equal for the baseline and PPS cases for $q_v \leq 600$ kPa
303 because the soil has not yet reached a strain softening condition. Beyond 600 kPa, the baseline
304 case indicates lower stiffness than the PPS case. Deformations for the LER case are close to the
305 baseline case for $q_v \leq 200$ kPa, and then deviate substantially with increasing applied vertical
306 stress. This suggests that, for the conditions simulated, a linearly elastic reinforcement model
307 can capture the deformation behavior of GRS bridge abutments at the service limit but not for
308 higher applied stress conditions approaching failure. As such, the selection of a constant

309 reinforcement stiffness value may be difficult. In the current study, the $J_{5\%}$ value (620 kN/m)
 310 gives good accuracy for $q_v \leq 200$ kPa.

311 Based on the data in Fig. 6, Table 4 provides values of maximum lateral facing
 312 displacement $\Delta_{h,200}$ and average abutment compression $\Delta_{v,200}$ at the service limit of $q_v = 200$
 313 kPa, vertical stress $q_{0.5\%}$ at the service limit of $\varepsilon_v = 0.5\%$, and vertical stress $q_{5\%}$ at the strength
 314 limit of $\varepsilon_v = 5\%$. Consistent with the trends in Fig. 5, the service limit values indicate
 315 essentially no effect for strain softening soil and a relatively minor effect for nonlinear
 316 reinforcement. In comparison, FHWA guidelines (Nicks et al. 2013) specify the allowable
 317 vertical stress at the service limit $q_{0.5\%}$ as 10% of the ultimate bearing capacity q_{ult} (Wu and
 318 Pham 2013, Wu et al. 2013), where q_{ult} is calculated as:

$$319 \quad q_{ult} = \left[\sigma'_c + 0.7 \frac{S_v}{S_v} \left(\frac{T_{ult}}{S_v} \right) \right] K_p + 2c' \sqrt{K_p} \quad (10)$$

320 and σ'_c = effective confining stress (typically taken as zero to be conservative), and K_p =
 321 Rankine passive earth pressure coefficient. Using Eq. (10) and $\sigma'_c = 0$, the calculated value of
 322 $q_{0.5\%}$ is 61 kPa for the baseline case, which is approximately one-half of the simulated value
 323 (118 kPa). Similar conservative results using Eq. (10) were reported by Nicks et al. (2016) for
 324 loading tests on GRS mini-piers constructed using a well-graded soil. At the strength limit of ε_v
 325 = 5%, the PPS simulation yielded a higher vertical stress by 14% and the LER simulation yielded
 326 a higher vertical stress by 75% than the baseline case. Thus, beyond the service limit, the effects
 327 of strain softening soil and nonlinear reinforcement can become significant and both should be
 328 taken into account as needed.

329

330 **Parametric Study**

331 A parametric study was conducted to investigate the effects of various reinforcement,
332 backfill soil, and geometry parameters on the deformation behavior of GRS bridge abutments.
333 The variables are reinforcement spacing, reinforcement stiffness, reinforcement length,
334 secondary reinforcement, backfill soil cohesion, backfill soil friction angle, backfill soil dilation
335 angle, bridge seat setback distance, bridge seat length, and abutment height. For each series of
336 simulations, only the variable of interest was changed and the other variables were held constant
337 and equal to the baseline case. Results are presented for maximum lateral facing displacement,
338 vertical compression, and vertical strain of the GRS bridge abutment with increasing average
339 applied vertical stress. A summary of values obtained at the service limit and strength limit is
340 presented in Table 5.

341

342 **Reinforcement Spacing**

343 Numerical simulations were conducted for reinforcement vertical spacing $S_v = 0.2$ m, 0.4
344 m, and 0.6 m. In each case, a soil lift thickness of 0.2 m was maintained for the numerical
345 construction procedure. Fig. 7 indicates that abutment deformations increase significantly with
346 increasing reinforcement spacing. For instance, at the service limit of $q_v = 200$ kPa, $\Delta_{h,200}$
347 increases from 38.0 mm to 93.6 mm and $\Delta_{v,200}$ increases from 33.6 mm to 70.2 mm when S_v
348 increases from 0.2 m to 0.6 m. At the service limit of $\varepsilon_v = 0.5\%$, the value of $q_{0.5\%} = 118$ kPa
349 for $S_v = 0.2$ m is nearly twice that for $S_v = 0.6$ m (65 kPa). At the strength limit, $q_{5\%}$ decreases
350 significantly and nonlinearly from 917 kPa to 519 kPa to 364 kPa when S_v increases from 0.2 m
351 to 0.4 m to 0.6 m.

352

353 **Reinforcement Stiffness**

354 Simulations were conducted for three HDPE geogrids, Geogrid-1, Geogrid-2 (baseline
355 case), and Geogrid-3, as originally described by Yu et al. (2016). Material properties are
356 provided in Table 2 and nonlinear tensile behavior is illustrated in Fig. 4. Geogrid-1 has the
357 lowest stiffness, Geogrid-2 is intermediate, and Geogrid-3 has the highest stiffness. Fig. 8
358 indicates that the maximum lateral facing displacement and vertical compression of the abutment
359 decrease significantly with increasing reinforcement stiffness. At $q_v = 200$ kPa, $\Delta_{h,200}$ decreases
360 from 47.6 mm to 30.7 mm and $\Delta_{v,200}$ decreases from 41.5 mm to 28.8 mm when reinforcement
361 changes from Geogrid-1 to Geogrid-3. Correspondingly, $q_{0.5\%}$ increases from 104 kPa to 143
362 kPa and $q_{5\%}$ increases from 500 kPa to 1121 kPa.

363

364 **Reinforcement Length**

365 Abutment deformations for reinforcement length $L_r = 0.3 h$, $0.5 h$, $0.7 h$, $0.9 h$, and 1.1
366 h are presented in Fig. 9 and decrease only slightly with increasing reinforcement length for L_r
367 $\geq 0.5 h$, which is consistent with the findings of Zheng and Fox (2016a) for service load
368 conditions. At the strength limit, $q_{5\%}$ increases from 898 kPa to 948 kPa when L_r increases
369 from $0.5 h$ to $1.1 h$. For $L_r = 0.3 h$ ($= 1.5$ m), the deformations are much larger than the other
370 cases and failure occurs at a lower applied vertical stress (523 kPa). In this case, the
371 reinforcement does not extend beyond the failure surface, which intersects the heel of the bridge
372 seat at the top of the wall (distance from wall facing $x = 1.7$ m).

373

374 **Secondary Reinforcement**

375 Secondary reinforcement layers often are included below the bridge seat to provide
376 additional support, and are specified for the GRS-IBS design method (Adams et al. 2011b). In
377 the current study, numerical simulations were conducted for secondary reinforcement layer
378 number $n_{sr} = 0, 5, 10,$ and $15,$ where $n_{sr} = 0$ indicates no secondary reinforcement and $n_{sr} = 15$
379 indicates 15 layers of secondary reinforcement between elevations $z = 2.0$ m and 5.0 m. The
380 secondary reinforcement layers have length $L_s + 2a_b$ ($= 1.9$ m) and are not connected to the
381 facing blocks. The results in Fig. 10 show that, when n_{sr} increases from 0 to 15, abutment
382 deformations are only slightly reduced for $q_v \leq 200$ kPa. At higher stress levels, abutment
383 deformations decrease significantly with an increasing number of secondary reinforcement layers.
384 For example, at the strength limit, $q_{5\%}$ increases from 917 kPa for $n_{sr} = 0$ to 1232 kPa for $n_{sr} =$
385 15. These results are consistent with the findings from large-scale loading tests on GRS mini-
386 piers, which indicate that secondary reinforcement is unlikely to reduce abutment compression
387 for service loads but can increase the ultimate bearing capacity (Nicks et al. 2013).

388

389 **Backfill Soil Cohesion**

390 Abutment deformations for backfill soil cohesion $c' = 0, 5$ kPa, 10 kPa, and 15 kPa are
391 presented in Fig. 11. Corresponding values of adhesion for soil-block and soil-geogrid interfaces
392 were obtained using Equation (9). The effect of increasing soil cohesion on abutment
393 deformations is small for service limit conditions, and becomes more important at higher stress
394 levels. As the cohesion increases from 0 to 15 kPa, $q_{0.5\%}$ increases from 118 kPa to 135 kPa and
395 $q_{5\%}$ increases from 917 kPa to 1008 kPa.

396

397 **Backfill Soil Friction Angle**

398 Simulations were conducted for backfill soil friction angle $\phi'_p = 38^\circ, 42^\circ, 46^\circ, \text{ and } 52^\circ$,
399 with $\phi'_{cv} = 35^\circ, 39^\circ, 43^\circ, \text{ and } 49^\circ$, respectively. Corresponding friction angles for soil-block and
400 soil-geogrid interfaces were obtained using Equation (9). The results in Fig. 12 indicate that
401 friction angle has a significant effect on abutment deformations, including both the service limit
402 and strength limit. For instance, $\Delta_{h,200}$ decreases from 51.4 mm to 34.3 mm and $\Delta_{v,200}$ decreases
403 from 40.7 mm to 31.2 mm when ϕ'_p increases from 38° to 52° . Correspondingly, $q_{0.5\%}$ increases
404 from 99 kPa to 127 kPa at the service limit of $\varepsilon_v = 0.5\%$ and $q_{5\%}$ increases from 682 kPa to
405 1059 kPa at the strength limit of $\varepsilon_v = 5\%$.

406

407 **Backfill Soil Dilation Angle**

408 Simulations were conducted for soil dilation angle $\psi_p = 6^\circ, 12^\circ, 18^\circ, \text{ and } 24^\circ$, and the
409 results are presented in Fig. 13. In general, maximum lateral facing displacements are not
410 significantly affected by dilation angle. Conversely, abutment vertical compression decreases
411 with increasing ψ_p , especially at higher stress levels. For instance, at the strength limit, $q_{5\%}$
412 increases from 777 kPa to 968 kPa when ψ_p increases from 6° to 24° .

413

414 **Bridge Seat Setback Distance**

415 Abutment deformations for bridge seat setback distance $a_b = 0.2 \text{ m}, 0.6 \text{ m}, 1.0 \text{ m}, \text{ and } 1.4$
416 m are presented in Fig. 14. Bridge seat setback has little effect on maximum lateral facing
417 displacement for $q_v \leq 600 \text{ kPa}$, whereas these values decrease with increasing a_b at higher

418 applied vertical stress levels. Similarly, abutment vertical compression decreases and $q_{5\%}$
419 increases from 917 kPa to 1127 kPa as a_b increases from 0.2 m to 1.4 m. The effect of bridge
420 seat setback is insignificant for service limit conditions.

421

422 **Bridge Seat Length**

423 Abutment deformations for bridge seat length $L_s = 1.0$ m, 1.5 m, 2.0 m, and 2.5 m are
424 presented in Fig. 15. Bridge seat length has little effect for service limit conditions. At higher
425 stress levels, the maximum lateral facing displacement and abutment compression generally
426 increase with increasing L_s . At the strength limit, $q_{5\%}$ decreases nonlinearly from 983 kPa to
427 917 kPa to 907 kPa when L_s increases from 1.0 m to 1.5 m to 2.0 m. However, for $L_s = 2.5$ m,
428 the maximum lateral displacement curve is similar to $L_s = 1.5$ m and the abutment compression
429 curve is similar to $L_s = 1.0$ m.

430

431 **Abutment Height**

432 Numerical simulations were conducted for GRS bridge abutments with height $h = 3$ m, 5
433 m, 7 m, and 9 m. Fig. 16 indicates that maximum lateral facing displacement and abutment
434 compression increase with increasing abutment height. For example, at $q_v = 200$ kPa, $\Delta_{h,200}$
435 increases from 26.7 mm to 60.6 mm and $\Delta_{v,200}$ increases from 23.9 mm to 43.1 mm when h
436 increases from 3 m to 9 m. Normalized relationships for maximum lateral facing displacement
437 divided by abutment height are shown in Fig. 16(c). The four relationships essentially converge
438 for $q_v \leq 200$ kPa and thus indicate that maximum lateral facing displacements are proportional to
439 abutment height for service limit conditions. Interestingly, at higher applied stress levels,

440 normalized maximum lateral facing displacement decreases as h increases from 3 m to 9 m for
441 the same applied vertical stress. Corresponding vertical stress-strain relationships, in which
442 abutment vertical compression is normalized by abutment height, are presented in Fig. 16(d) and
443 show similar trends. Thus, taller abutments have a stiffer response. This is attributed to higher
444 average effective stress conditions and associated larger soil stiffness for the taller abutments.
445 The results in Fig. 16(c) and Fig. 16(d) suggest that, all else being equal, laboratory or field tests
446 conducted on reduced-scale physical models with lower average effective stress conditions may
447 yield conservative (i.e., less stiff) vertical stress-strain relationships for the design of GRS bridge
448 abutments.

449

450 **Failure Surface**

451 The failure surface for the GRS bridge abutment develops as shear strains increase during
452 the loading stage. Contours of shear strain magnitude for the baseline case at the service limit
453 ($\varepsilon_v = 0.5\%$) and strength limit ($\varepsilon_v = 5\%$) are shown in Fig. 17. At the service limit, shear strains
454 are concentrated at the heel of the bridge seat and suggest a potential failure surface that moves
455 downward from the heel to the toe of the abutment. At the strength limit, the abutment is
456 approaching failure as manifested by the formation of large shear strain zones. The failure
457 mechanism is a combination of punching shear failure of the bridge seat and internal shear
458 failure of the GRS bridge abutment. The internal failure surface migrates vertically downward
459 from the heel of the bridge seat to approximately the mid-height of the abutment, and then
460 diagonally to the toe of the abutment. A similar failure surface shape for GRS bridge abutments
461 was identified by Leshchinsky (2014) based on limit analysis.

462 Following an approach similar to Fig. 17(b), a bilinear failure surface was constructed at
463 the strength limit for each simulation of the parametric study based on contours of shear strain
464 magnitude. These simplified diagrams are presented together for comparison in Fig. 18. In
465 general, the geometry of these surfaces show close similarity over a wide range of simulated
466 conditions, with some exceptions. The bilinear surface consistently starts at the heel of bridge
467 seat and migrates downward to the mid-height of the GRS bridge abutment and then diagonally
468 to the toe of the abutment. Failure surfaces show essentially no effect from changing vertical
469 reinforcement spacing in Fig. 18(a), and similar close agreement for variable geogrid stiffness
470 and geogrid length in Fig. 18(b) and Fig. 18(c), respectively. The failure surfaces in Fig. 18(d)
471 indicate that the intersection point of the bilinear surface moves downward with increasing
472 number of secondary reinforcement layers, as might be expected. The failure surfaces in Figs.
473 18 (e)–(g) indicate that backfill soil cohesion, friction angle, and dilation angle have little effect
474 on failure surface geometry. Conversely, the failure surfaces in Figs. 18(h)–(j) show that
475 abutment geometry has an important effect. Fig. 18(h) indicates that increasing the bridge seat
476 setback distance changes the slope of the upper line of the bilinear failure surface but,
477 interestingly, has no effect on the intersection point or lower line for the conditions investigated.
478 Fig. 18(i) indicates that increasing the bridge seat length changes the geometry for both sections
479 of the failure surface but the vertical elevation of the intersection point remains consistent.
480 Finally, Fig. 18(j) indicates that abutments with heights of 5 m, 7 m, and 9 m have the same
481 relative geometry when plotted as z/h ; however, the lower height of $h = 3$ m displays a clearly
482 different geometry that is similar to the failure surfaces for abutments with larger a_b and L_s .

483 Based on the trends in Fig. 18, a general bilinear failure surface is proposed and
484 illustrated in Fig. 19 for GRS bridge abutments with conditions similar to those investigated in

485 the current study. The failure surface starts at the heel of the bridge seat and moves downward to
486 an intersection point at mid-height ($z = h/2$) and then diagonally to the toe of the abutment.
487 The horizontal location of the intersection point is controlled by geometry. For $a_b + L_s \leq h/3$,
488 the upper line is vertical and the intersection point is located at $x = a_b + L_s$. For $a_b + L_s > h/3$,
489 the upper line is not vertical and the intersection point is located at $x = h/3$. The proposed
490 failure surface is predicated on the assumption that secondary reinforcement, if present, is
491 contained within the top half of the abutment.

492

493 **Conclusions**

494 A numerical investigation of deformation and failure behavior for geosynthetic reinforced
495 soil (GRS) bridge abutments was conducted using finite difference analysis. The backfill soil
496 was characterized using a nonlinear elasto-plastic model that incorporates a hyperbolic stress-
497 strain relationship with strain softening behavior and the Mohr-Coulomb failure criterion. The
498 geogrid reinforcement was characterized using a hyperbolic load-strain-time model. For each
499 numerical simulation, the GRS bridge abutment model was constructed in stages, including soil
500 compaction effects, and then monotonically loaded in stages to failure. A parametric study was
501 conducted to investigate the effects of various parameters on abutment deformation and failure
502 behavior. The following conclusions are reached for the conditions investigated in this study:

503

504 1. As compared to simulations for elastic-perfectly plastic soil and linearly elastic
505 reinforcement, strain softening behavior of the backfill soil and nonlinear behavior of the
506 geogrid reinforcement had relatively small effects on abutment deformations at the service
507 limit ($\varepsilon_v = 0.5\%$ or $q_v = 200$ kPa). However, these effects, and especially nonlinear

508 reinforcement, became significant above the service limit leading to the strength limit ($\varepsilon_v =$
509 5%). A linearly elastic reinforcement model was able to characterize deformation behavior
510 of GRS bridge abutments at the service limit, but not for higher applied vertical stress
511 conditions approaching failure. Bearing capacity at the strength limit was slightly
512 overestimated using a perfectly plastic soil model and significantly overestimated using a
513 linearly elastic reinforcement model.

514 2. Reinforcement spacing, reinforcement stiffness, backfill soil friction angle, and abutment
515 height had the most significant effects on abutment deformations. The maximum lateral
516 facing displacement and abutment vertical compression decreased significantly with
517 decreasing reinforcement spacing, increasing reinforcement stiffness, and increasing backfill
518 soil friction angle. As abutment height increased, the maximum lateral facing displacement
519 and abutment vertical compression increased; however, the normalized maximum lateral
520 facing displacement and vertical strain decreased. Secondary reinforcement had a relatively
521 small effect at the service limit and significantly increased the bearing capacity at the
522 strength limit.

523 3. Reinforcement and backfill soil properties had little effect on the geometry of the failure
524 surface. Conversely, parameters associated with abutment geometry, such as bridge seat
525 length, bridge seat setback distance, and abutment height, had important effects. The failure
526 surface can be approximated as bilinear, starting at the heel of the bridge seat, moving
527 downward to an intersection point at mid-height of the abutment, and then diagonally to the
528 toe of the abutment, as illustrated in Fig. 19.

529

530 **Acknowledgements**

531 Financial support for this investigation was provided by the California Department of
532 Transportation (Caltrans) and is gratefully acknowledged. The authors thank Dr. Charles S.
533 Sikorsky of the Caltrans Office of Earthquake Engineering for his support and assistance with
534 the project and Dr. P. Benson Shing, Professor and Chair of the Department of Structural
535 Engineering at University of California, San Diego, for several helpful discussions on the design
536 of bridge systems.

537

538 Notation

539 *The following symbols are used in this paper:*

540 A_r = reinforcement cross-sectional area

541 a_b = bridge seat setback distance

542 B = bulk modulus

543 c' = soil cohesion

544 c'_i = interface adhesion

545 D = bridge beam depth

546 d_{max} = soil maximum particle size

547 d_e = distance between top facing block and bridge beam

548 E = elastic modulus

549 E_r = reinforcement elastic modulus

550 E_t = soil tangent elastic modulus

551 E_{ur} = soil unloading-reloading elastic modulus

552 F_v = vertical force per unit width on bridge abutment

- 553 h = abutment height
- 554 J_t = reinforcement tangent stiffness
- 555 J_s = reinforcement secant stiffness
- 556 J_0 = reinforcement initial stiffness
- 557 $J_{5\%}$ = reinforcement secant stiffness at 5% strain
- 558 K = elastic modulus number
- 559 K_b = bulk modulus number
- 560 k_n = interface normal stiffness
- 561 K_p = Rankine passive earth pressure coefficient
- 562 k_s = interface shear stiffness
- 563 K_{ur} = unloading-reloading modulus number
- 564 L_b = bridge span
- 565 L_c = contact length between bridge beam and bridge seat
- 566 L_s = bridge seat length
- 567 L_r = reinforcement length
- 568 m = bulk modulus exponent
- 569 n = elastic modulus exponent
- 570 n_{sr} = number of secondary reinforcement layers
- 571 p_a = atmospheric pressure
- 572 q_{ult} = ultimate bearing capacity

- 573 q_v = average applied vertical stress on GRS bridge abutment
- 574 $q_{0.5\%}$ = average applied vertical stress on GRS bridge abutment at 0.5% strain
- 575 $q_{5\%}$ = average applied vertical stress on GRS bridge abutment at 5% strain
- 576 RF = interface shear strength reduction factor
- 577 R_f = failure ratio
- 578 R_{sd} = ratio of bridge beam span to bridge beam depth
- 579 S_v = reinforcement vertical spacing
- 580 T = reinforcement tensile force
- 581 T_{ult} = reinforcement ultimate tensile strength
- 582 $T_{5\%}$ = reinforcement tensile force at 5% strain
- 583 t = time
- 584 t_r = reinforcement thickness
- 585 x = horizontal distance from back side of wall facing
- 586 z = vertical distance above top surface of foundation soil
- 587 χ = empirical fitting parameter
- 588 $\Delta_{h,200}$ = maximum lateral facing displacement for $q_v = 200$ kPa
- 589 $\Delta_{v,200}$ = average abutment compression for $q_v = 200$ kPa
- 590 δ'_i = interface friction angle
- 591 ε = reinforcement tensile strain
- 592 ε_p = soil incremental plastic shear strain
- 593 ε_v = average abutment vertical strain

- 594 ϕ' = soil friction angle
- 595 ϕ'_{cv} = soil constant volume friction angle
- 596 ϕ'_p = soil peak friction angle
- 597 γ = soil unit weight
- 598 γ_b = bridge beam unit weight
- 599 ν = Poisson's ratio
- 600 ν_t = tangent Poisson's ratio
- 601 σ'_c = effective confining stress
- 602 σ'_1 = major principal effective stress
- 603 σ'_3 = minor principal effective stress
- 604 ψ = soil dilation angle
- 605 ψ_{cv} = soil constant volume dilation angle
- 606 ψ_p = soil peak dilation angle

607

608 **References**

- 609 Abu-Hejleh, N., Outcalt, W., Wang, T., and Zornberg, J. G. (2000). "Performance of
610 geosynthetic-reinforced walls supporting the Founders/Meadows Bridge and approaching
611 roadway structures. Report 1: Design, materials, construction, instrumentation and
612 preliminary results." *Report No. CDOT-DTD-R-2000-5*, Colorado DOT, Denver, CO.
- 613 Abu-Hejleh, N., Zornberg, J. G., Wang, T., McMullen, M., and Outcalt, W. (2001).
614 "Performance of geosynthetic-reinforced walls supporting the Founders/Meadows Bridge

- 615 and approaching roadway structures. Report 2: Assessment of the performance and design of
616 the front GRS walls and recommendations for future GRS bridge abutments.” *Report No.*
617 *CDOT-DTD-R-2001-12*, Colorado DOT, Denver, CO.
- 618 Abu-Hejleh, N., Zornberg, J. G., Wang, T., and Watcharamonthein, J. (2002). “Monitored
619 displacements of unique geosynthetic-reinforced soil bridge abutments.” *Geosynthetics*
620 *International*, Vol. 9, No. 1, 71-95.
- 621 Adams, M. (1997). “Performance of a prestained geosynthetic reinforced soil bridge pier.”
622 *Mechanically Stabilized Backfill*, Balkema, Rotterdam, Netherlands, 35-53.
- 623 Adams, M., Nicks, J., Stabile, T., Wu, J., Schlatter, W., and Hartmann, J. (2011a). “Geosynthetic
624 reinforced soil integrated bridge system synthesis report.” *FHWA-HRT-11-027*, U.S. DOT,
625 Washington, D.C.
- 626 Adams, M., Nicks, J., Stabile, T., Wu, J., Schlatter, W., and Hartmann, J. (2011b). “Geosynthetic
627 reinforced soil integrated bridge system interim implementation guide.” *FHWA-HRT-11-026*,
628 U.S. DOT, Washington, D.C.
- 629 Adams, M. T., Ooi, P. S., and Nicks, J. E. (2014). “Mini-pier testing to estimate performance of
630 full-scale geosynthetic reinforced soil bridge abutments.” *Geotechnical Testing Journal*, Vol.
631 37, No. 5, 884-894.
- 632 Allen, T. M., and Bathurst, R. J. (2014a). “Design and performance of 6.3-m-high, block-faced
633 geogrid wall designed using K-stiffness method.” *Journal of Geotechnical and*
634 *Geoenvironmental Engineering*, Vol. 142, No. 2, 04013016.
- 635 Allen, T. M., and Bathurst, R. J. (2014b). “Performance of an 11 m high block-faced geogrid
636 wall designed using the K-stiffness method.” *Canadian Geotechnical Journal*, Vol. 51, No.
637 1, 16-29.

- 638 Ambauen, S., Leshchinsky, B., Xie, Y., and Rayamajhi, D. (2015). "Service-state behavior of
639 reinforced soil walls supporting spread seats: a parametric study using finite-element
640 analysis." *Geosynthetics International*, Vol. 23, No. 3, 156-170.
- 641 Ardah, A., Abu-Farsakh, M., and Voyiadjis, G. (2017). "Numerical evaluation of the
642 performance of a Geosynthetic Reinforced Soil-Integrated Bridge System (GRS-IBS) under
643 different loading conditions." *Geotextiles and Geomembranes*, Vol. 45, No. 6, 558-569.
- 644 Berg, R. R., Christopher, B. R., and Samtani, N. (2009). "Design and construction of
645 mechanically stabilized earth walls and reinforced soil slopes – Volume I." *FHWA-NHI-10-*
646 *024*, U.S. DOT, Washington, D.C.
- 647 Caltrans (1994). "Memos to Designers 7-1." California DOT, Sacramento, CA.
- 648 Duncan, J. M., Byrne, P., Wong, K. S., and Mabry, P. (1980). "Strength, stress-strain and bulk
649 modulus parameters for finite element analysis of stresses and movements in soil masses."
650 *Report No. UCB/GT/80-01*, University of California, Berkeley, CA, USA.
- 651 *FLAC2D Version 7.0* [Computer software]. (2011). Itasca Consulting Group, Minneapolis, MN,
652 USA.
- 653 Gotteland, P., Gourc, J. P., and Villard, P. (1997). "Geosynthetic reinforced structures as bridge
654 abutments: Full scale experimentation and comparison with modelisations." *Mechanically*
655 *Stabilized Backfill*, Balkema, Rotterdam, Netherlands, 25-34.
- 656 Guler, E., Hamderi, M., and Demirkan, M. M. (2007). "Numerical analysis of reinforced soil-
657 retaining wall structures with cohesive and granular backfills." *Geosynthetics International*,
658 Vol. 14, No. 6, 330–345.

- 659 Hatami, K., and Bathurst, R. J. (2006). "Numerical model for reinforced soil segmental walls
660 under surcharge loading." *Journal of Geotechnical and Geoenvironmental Engineering*, Vol.
661 132, No. 6, 673-684.
- 662 Helwany, S. M. B., Wu, J. T. H., and Froessl, B. (2003). "GRS bridge abutments – An effective
663 means to alleviate bridge approach settlement." *Geotextiles and Geomembranes*, Vol. 21, No.
664 3, 177-196.
- 665 Helwany, S. M. B., Wu, J. T. H., and Kitsabunnarat, A. (2007). "Simulating the behavior of GRS
666 bridge abutments." *Journal of Geotechnical and Geoenvironmental Engineering*, Vol. 133,
667 No. 10, 1229-1240.
- 668 Huang, B., Bathurst, R. J., Hatami, K., and Allen, T. M. (2010). "Influence of toe restraint on
669 reinforced soil segmental walls." *Canadian Geotechnical Journal*, Vol. 47, No. 8, 885-904.
- 670 Iwamoto, M. K., Ooi, P. S., Adams, M. T., and Nicks, J. E. (2015). "Composite properties from
671 instrumented load tests on mini-piers reinforced with geotextiles." *Geotechnical Testing*
672 *Journal*, Vol. 38, No. 4, 397-408.
- 673 Ketchart, K., and Wu, J. T. H. (1997). "Performance of geosynthetic-reinforced soil bridge pier
674 and abutment, Denver, Colorado, USA." *Mechanically Stabilized Backfill*, Balkema,
675 Rotterdam, Netherlands, 101-116.
- 676 Lee, K. Z. Z., and Wu, J. T. H. (2004). "A synthesis of case histories on GRS bridge-supporting
677 structures with flexible facing." *Geotextiles and Geomembranes*, Vol. 22, No. 4, 181-204.
- 678 Leshchinsky, B. (2014). "Limit analysis optimization of design factors for mechanically
679 stabilized earth wall-supported seats." *Transportation Infrastructure Geotechnology*, Vol. 1,
680 No. 2, 111-128.

- 681 Ling, H. I., Yang, S., Leshchinsky, D., Liu, H., and Burke, C. (2010). "Finite-element
682 simulations of full-scale modular-block reinforced soil retaining walls under earthquake
683 loading." *Journal of Engineering Mechanics*, Vol. 136, No. 5, 653-661.
- 684 Liu, H., and Ling, H. I. (2012). "Seismic responses of reinforced soil retaining walls and the
685 strain softening of backfill soils." *International Journal of Geomechanics*, Vol. 12, No. 4,
686 351-356.
- 687 Nicks, J. E., Adams, M. T., Ooi, P. S. K., and Stabile, T. (2013). "Geosynthetic reinforced soil
688 performance testing – axial load deformation relationships." *FHWA-HRT-13-066*, U.S. DOT,
689 Washington, D.C.
- 690 Nicks, J. E., Esmaili, D., and Adams, M. T. (2016). "Deformations of geosynthetic reinforced
691 soil under bridge service loads." *Geotextiles and Geomembranes*, Vol. 44, No. 4, 641-653.
- 692 Saghebfar, M., Abu-Farsakh, M., Ardah, A., and Chen, Q. (2017). "Performance monitoring of
693 Geosynthetic Reinforced Soil Integrated Bridge System (GRS-IBS) in Louisiana."
694 *Geotextiles and Geomembranes*, Vol. 45, No. 2, 34-47.
- 695 Stein, W. J., and Neuman, T. R. (2007). *Mitigation strategies for design exceptions*. FHWA-SA-
696 07-011, U.S. DOT, Washington, D.C.
- 697 Vieira, C. S., Lopes, M. L., and Caldeira, L. M. (2013). "Sand–geotextile interface
698 characterisation through monotonic and cyclic direct shear tests." *Geosynthetics
699 International*, Vol. 20, No. 1, 26-38.
- 700 Walters, D. L., Allen, T. M., and Bathurst, R. J. (2002). "Conversion of geosynthetic strain to
701 load using reinforcement stiffness", *Geosynthetics International*, Vol. 9, Nos. 5-6, 483-523.

- 702 Won, G. W., Hull, T., and De Ambrosis, L. (1996). "Performance of a geosynthetic segmental
703 block wall structure to support bridge abutments." *Earth Reinforcement*, Vol. 1, Balkema,
704 Rotterdam, Netherlands, 543–548.
- 705 Wu, J. T. H., Ketchart, K., and Adams, M. (2001). "GRS bridge piers and abutments." *Report*
706 *No. FHWA-RD-00-038*, U.S. DOT, Washington, D.C.
- 707 Wu, J. T. H., Lee, K. Z. Z., Helwany, S. B., and Ketchart, K. (2006a). "Design and construction
708 guidelines for geosynthetic-reinforced soil bridge abutments with a flexible facing." *NCHRP*
709 *Report 556*, Transportation Research Board, Washington, D.C.
- 710 Wu, J. T. H., Lee, K. Z. Z., and Pham, T. (2006b). "Allowable bearing pressures of bridge sills
711 on GRS bridge abutments with flexible facing." *Journal of Geotechnical and*
712 *Geoenvironmental Engineering*, Vol. 132, No. 7, 830-841.
- 713 Wu, J. T. H., and Pham, T. Q. (2013). "Load-carrying capacity and required reinforcement
714 strength of closely spaced soil-geosynthetic composites." *Journal of Geotechnical and*
715 *Geoenvironmental Engineering*, Vol. 139, No. 9, 1468-1476.
- 716 Wu, J. T. H., Pham, T. Q., and Adams, M. T. (2013). "Composite behavior of geosynthetic
717 reinforced soil mass." *FHWA-HRT-10-077*, U.S. DOT, Washington, D.C.
- 718 Xie, Y., and Leshchinsky, B. (2015). "MSE walls as bridge abutments: Optimal reinforcement
719 density." *Geotextiles and Geomembranes*, Vol. 43, No. 2, 128-138.
- 720 Yang, K. -H., Zornberg, J. G., Liu, C.-N., and Lin, H.-D. (2012). "Stress distribution and
721 development within geosynthetic-reinforced soil slopes." *Geosynthetics International*, Vol.
722 19, No. 1, 62–78.

- 723 Yu, Y., Bathurst, R. J., and Allen, T. M. (2016). "Numerical modeling of the SR-18 geogrid
724 reinforced modular block retaining walls." *Journal of Geotechnical and Geoenvironmental*
725 *Engineering*, 10.1061/(ASCE)GT.1943-5606.0001438, 04016003.
- 726 Zheng, Y., and Fox, P. J. (2016a). "Numerical investigation of geosynthetic-reinforced soil
727 bridge abutments under static loading." *Journal of Geotechnical and Geoenvironmental*
728 *Engineering*, 10.1061/(ASCE)GT.1943-5606.0001452, 04016004.
- 729 Zheng, Y., and Fox, P. J. (2016b). Closure to "Numerical investigation of geosynthetic-
730 reinforced soil bridge abutments under static loading." By Yewei Zheng, and Patrick J. Fox.
731 *Journal of Geotechnical and Geoenvironmental Engineering*, 10.1061/(ASCE)GT.1943-
732 5606.0001623, 07016032.
- 733 Zheng, Y., and Fox, P. J. (2017). "Numerical investigation of the geosynthetic reinforced soil-
734 integrated bridge system under static loading." *Journal of Geotechnical and*
735 *Geoenvironmental Engineering*, 10.1061/(ASCE)GT.1943-5606.0001665, 04017008.
- 736 Zheng, Y., Fox, P. J., and McCartney, J. S. (2017). "Numerical study of compaction effect on the
737 static behavior of geosynthetic reinforced soil-integrated bridge system." *Geotechnical*
738 *Frontiers 2017*, Orlando, FL, USA, 33-43.
- 739 Zheng, Y., Fox, P. J., and Shing, P. B. (2014). "Numerical simulations for response of MSE
740 wall-supported bridge abutment to vertical load." *GeoShanghai 2014, International*
741 *Conference on Geotechnical Engineering 2014*, ASCE, Reston, VA, USA, 493-502.
- 742 Zheng, Y., Fox, P. J., and Shing, P. B. (2015). "Numerical study of deformation behavior for a
743 geosynthetic-reinforced soil bridge abutment under static loading." *IFCEE 2015,*
744 *International Foundations Congress & Equipment Exposition 2015*, ASCE, Reston, VA,
745 USA, 1503-1512.

List of Table Captions

Table 1. Soil parameters.

Table 2. Reinforcement parameters.

Table 3. Interface parameters.

Table 4. Deformations and vertical stresses for three simulation cases at the service limit and strength limit.

Table 5. Results from parametric study at the service limit and strength limit.

Table 1. Soil parameters.

Property	Value
<u>Backfill Soil</u>	
Unit weight, γ (kN/m ³)	17.3
Elastic modulus number, K	334
Unloading-reloading elastic modulus number, K_{ur}	401
Elastic modulus exponent, n	0.66
Failure ratio, R_f	0.67
Bulk modulus number, B	254
Bulk modulus exponent, m	0
Atmospheric pressure, p_a (kPa)	101.3
Cohesion, c' (kPa)	0
Peak friction angle, ϕ'_p (°)	46
Constant volume friction angle, ϕ'_{cv} (°)	43
Peak dilation angle, ψ_p (°)	18
Constant volume dilation angle, ψ_{cv} (°)	0
<u>Foundation Soil</u> ^a	
Unit weight, γ (kN/m ³)	21.7
Elastic modulus, E (MPa)	80
Poisson's ratio, ν	0.3
Cohesion, c' (kPa)	2
Friction angle, ϕ' (°)	54
Dilation angle, ψ (°)	14

^a from Yu et al. (2016).

Table 2. Reinforcement parameters.

Property	Geogrid-1	Geogrid-2	Geogrid-3
Elastic modulus, E_r	Variable ^a	Variable ^a	Variable ^a
Cross-sectional area, A_r	0.002 m ²	0.002 m ²	0.002 m ²
Thickness, t_r	2 mm	2 mm	2 mm
Tensile strength @5% strain, $T_{5\%}$ ^b	27 kN/m	31 kN/m	52 kN/m
Ultimate tensile strength, T_{ult} ^b	58 kN/m	70 kN/m	114 kN/m
Initial tensile stiffness, J_0 ^c	524 kN/m	596 kN/m	1085 kN/m
Fitting parameter, χ ^c	0.0958 m/kN	0.0359 m/kN	0.0326 m/kN

^a Calculated using Eqs. (7-8) based on parameters reported by Yu et al. (2016).

^b Provided by manufacturer.

^c Calculated for $t = 3600$ hours.

Table 3. Interface parameters.

Property	Soil-geogrid	Soil-block/bridge seat	Block-block	Bridge beam-bridge seat
Normal stiffness, k_n	-	1,000 MPa/m	100,000 MPa/m	100,000 MPa/m
Shear stiffness, k_s	1 MN/m/m	1 MPa/m	40 MPa/m	40 MPa/m
Friction angle, δ'_i	41.4° ^a	33.9° ^b	36.0° ^c	21.8° ^d
Adhesion, c'_i	0	0	58 kPa ^c	0

^a Based on average of data ($RF = 0.85$) from Vieira et al. (2013).

^b Based on data ($RF = 0.65$) from Ling et al. (2010).

^c Based on Yu et al. (2016).

^d Based on a friction coefficient of 0.4 for bearing pads from Caltrans (1994).

Table 4. Deformations and vertical stresses for three simulation cases at the service limit and strength limit.

Case	Service limit			Strength limit
	$\Delta_{h,200}$ (mm)	$\Delta_{v,200}$ (mm)	$q_{0.5\%}$ (kPa)	$q_{5\%}$ (kPa)
Baseline	38.0	33.6	118	917
Perfectly plastic soil	38.0	33.6	118	1043
Linearly elastic reinforcement	35.2	31.3	127	1600

Table 5. Results from parametric study at the service limit and strength limit.

		Service limit			Strength limit
		$\Delta_{h,200}$ (mm)	$\Delta_{v,200}$ (mm)	$q_{0.5\%}$ (kPa)	$q_{5\%}$ (kPa)
Reinforcement spacing	0.2 m	38.0	33.6	118	917
	0.4 m	60.5	48.0	82	519
	0.6 m	93.6	70.2	65	364
Reinforcement stiffness	Geogrid-1	47.6	41.5	104	500
	Geogrid-2	38.0	33.6	118	917
	Geogrid-3	30.7	28.8	143	1121
Reinforcement length	0.3 <i>h</i>	65.4	46.8	101	523
	0.5 <i>h</i>	40.3	34.5	115	898
	0.7 <i>h</i>	38.0	33.6	118	917
	0.9 <i>h</i>	37.5	33.5	119	925
	1.1 <i>h</i>	37.5	33.5	119	948
Secondary reinforcement layers	0	38.0	33.6	118	917
	5	37.0	32.7	123	1007
	10	35.0	31.6	127	1117
	15	34.0	30.9	131	1232
Backfill soil cohesion	0 kPa	38.0	33.6	118	917
	5 kPa	35.3	32.7	124	940
	10 kPa	33.6	31.5	127	975
	15 kPa	33.0	31.0	135	1008
Backfill soil friction angle	38°	51.4	40.7	99	682
	42°	43.7	36.9	108	805
	46°	38.0	33.6	118	917
	50°	34.3	31.2	127	1059
Backfill soil dilation angle	6°	39.4	39.7	105	777
	12°	38.7	36.0	113	852
	18°	38.0	33.6	118	917
	24°	38.0	32.3	123	968
Bridge seat setback distance	0.2 m	38.0	33.6	118	917
	0.6 m	40.0	32.5	131	962
	1.0 m	39.1	30.8	146	1040
	1.4 m	38.5	28.2	157	1127
Bridge seat length	1.0 m	35.4	29.0	127	983
	1.5 m	38.0	33.6	118	917
	2.0 m	40.9	37.7	115	907
	2.5 m	42.3	38.5	115	980
Abutment height	3.0 m	26.7	23.9	143	926
	5.0 m	38.0	33.6	118	917
	7.0 m	49.2	39.9	137	1008
	9.0 m	60.6	43.1	158	1049

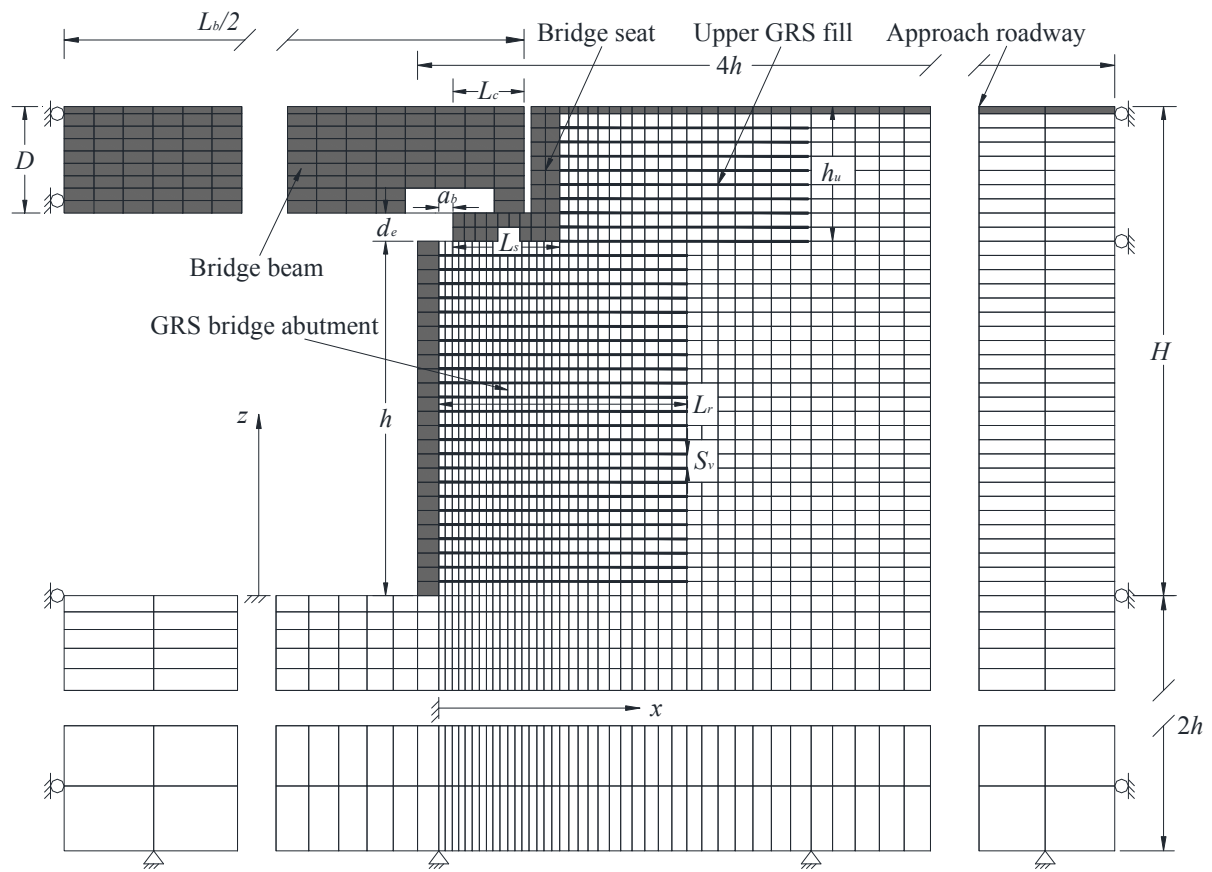
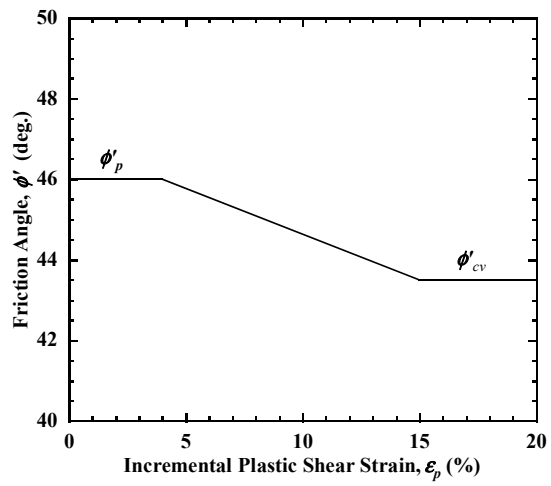
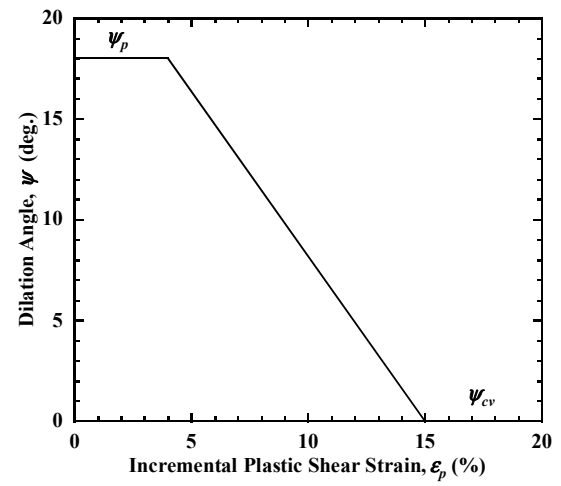


Fig. 1. Finite difference grid and boundary conditions for GRS bridge abutment baseline case.



(a)



(b)

Fig. 2. Relationships for soil parameters with incremental plastic shear strain: (a) friction angle; (b) dilation angle.

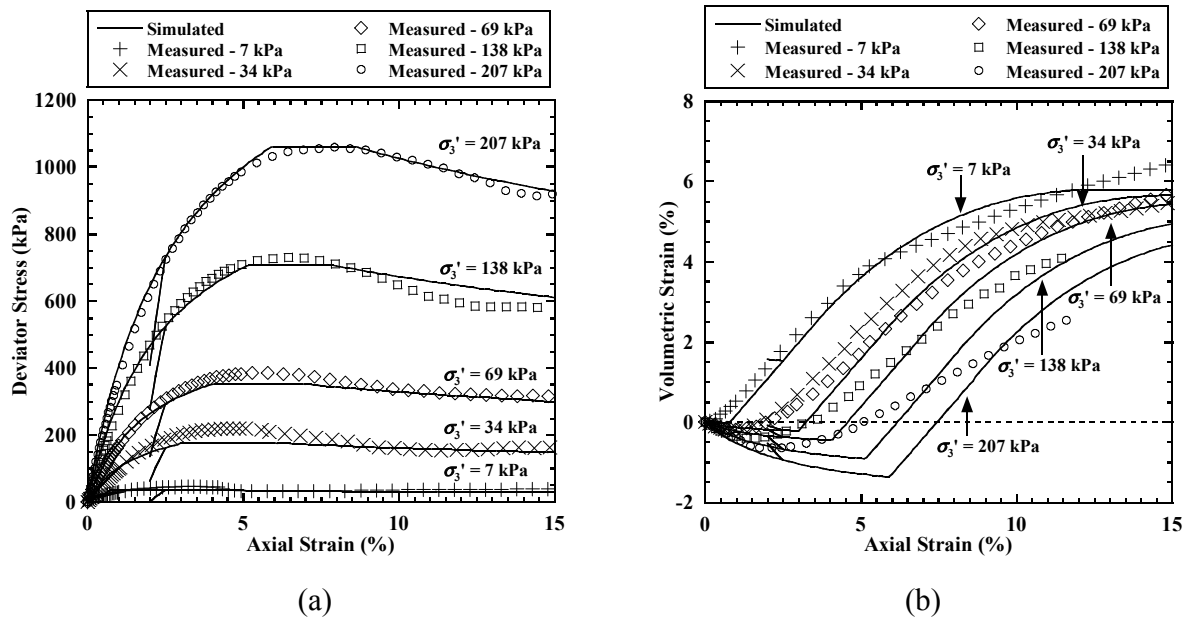


Fig. 3. Comparison of measured and simulated triaxial test results: (a) deviator stress vs. axial strain; (b) volumetric strain vs. axial strain.

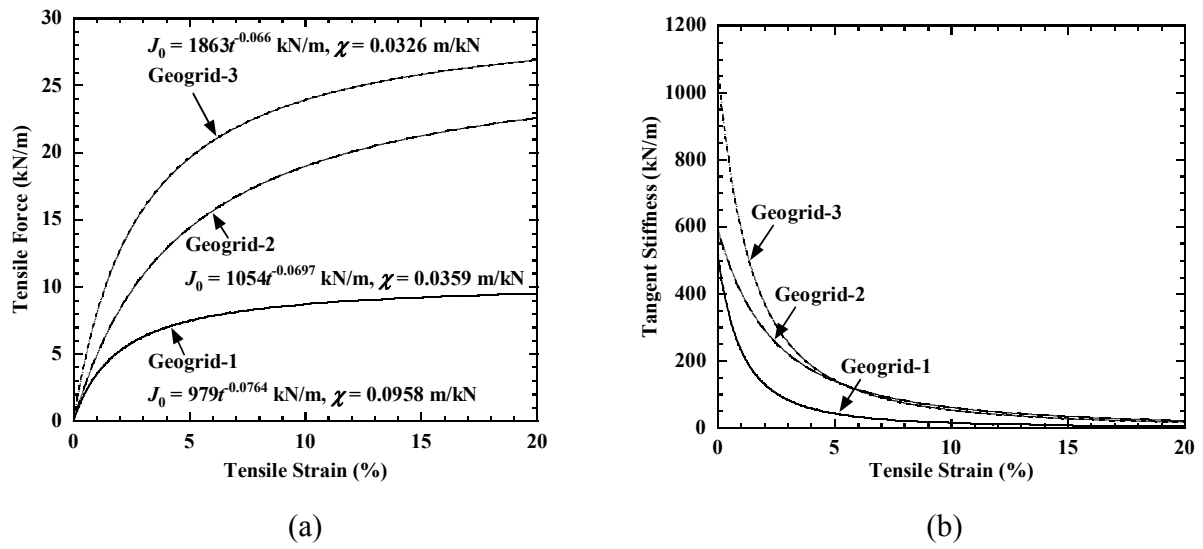


Fig. 4. Tensile behavior for three HDPE geogrids at $t = 3600$ hours: (a) tensile force-strain relationship; (b) tangent stiffness (parameters from Yu et al. 2016).

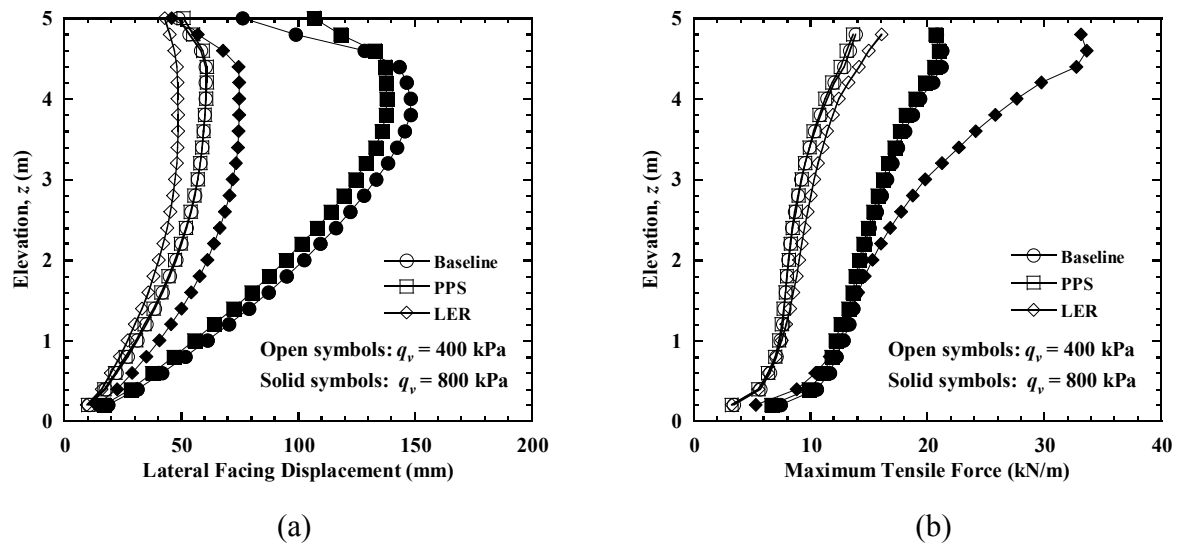


Fig. 5. Simulation results for $q_v = 400$ kPa and $q_v = 800$ kPa: (a) lateral facing displacement; (b) maximum tensile force in reinforcement.

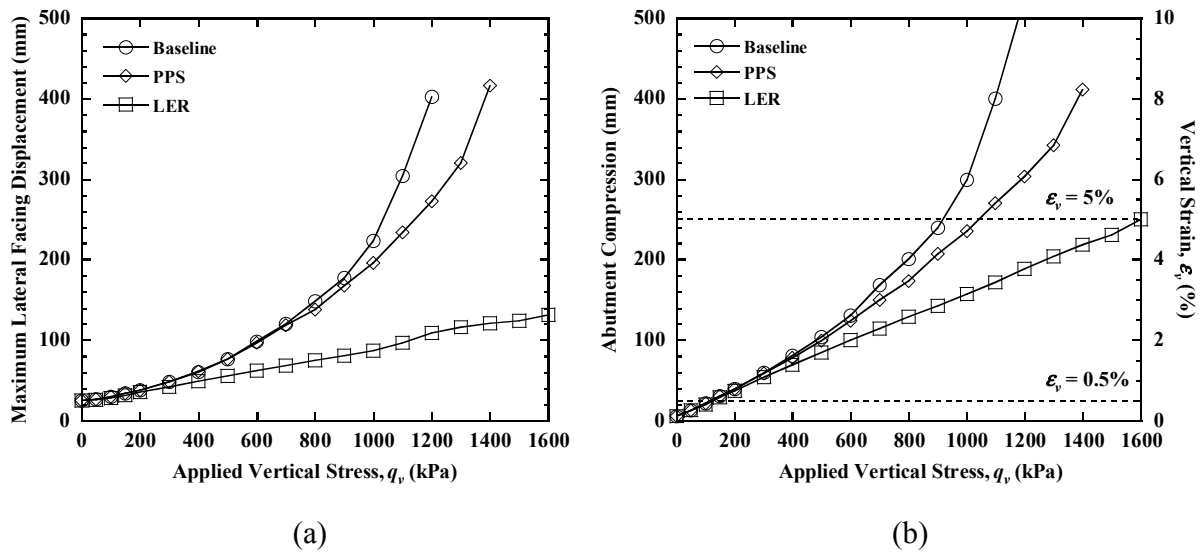


Fig. 6. Simulation results: (a) maximum lateral facing displacement; (b) abutment compression and vertical strain.

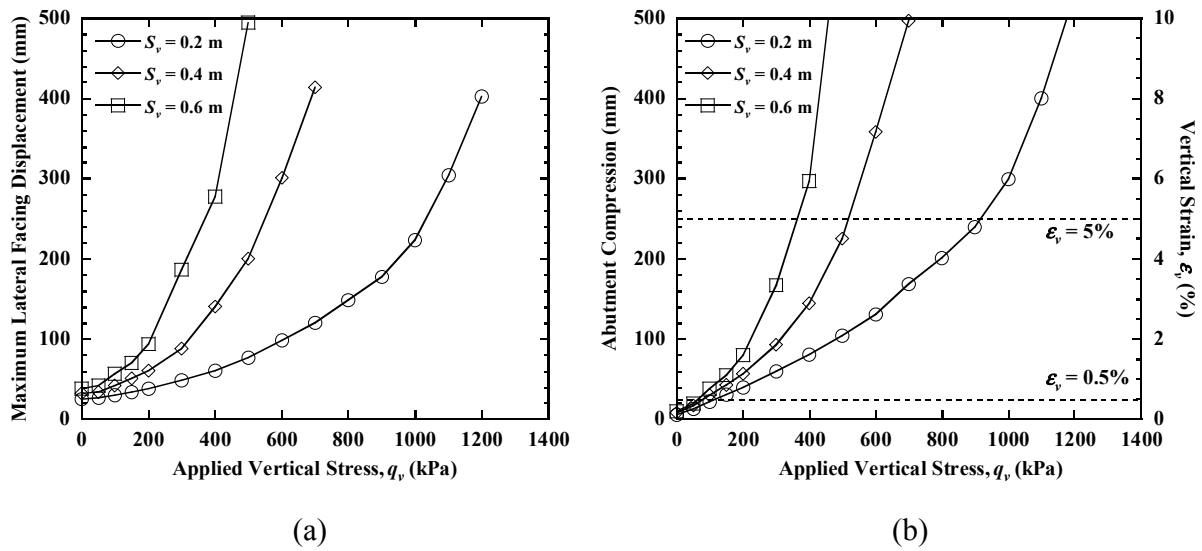


Fig. 7. Effect of reinforcement spacing: (a) maximum lateral facing displacement; (b) abutment compression and vertical strain.

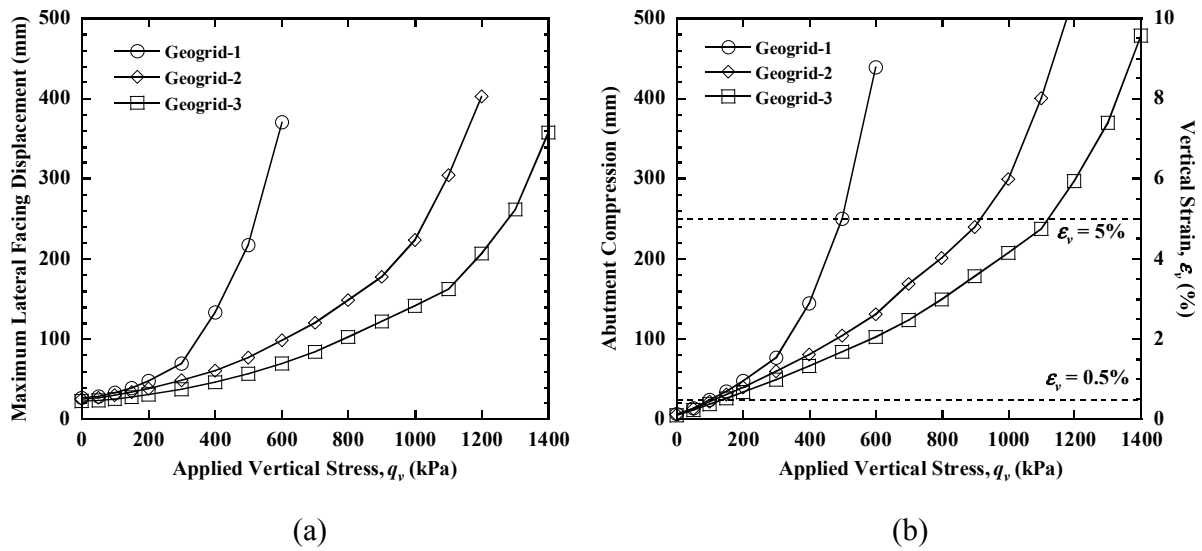


Fig. 8. Effect of reinforcement stiffness: (a) maximum lateral facing displacement; (b) abutment compression and vertical strain.

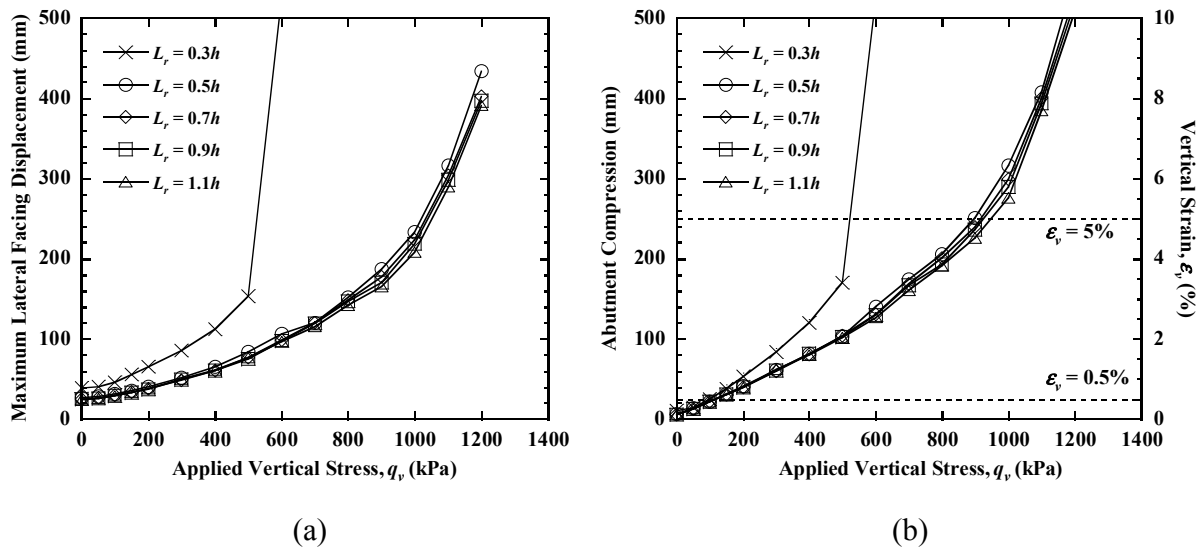


Fig. 9. Effect of reinforcement length: (a) maximum lateral facing displacement; (b) abutment compression and vertical strain.

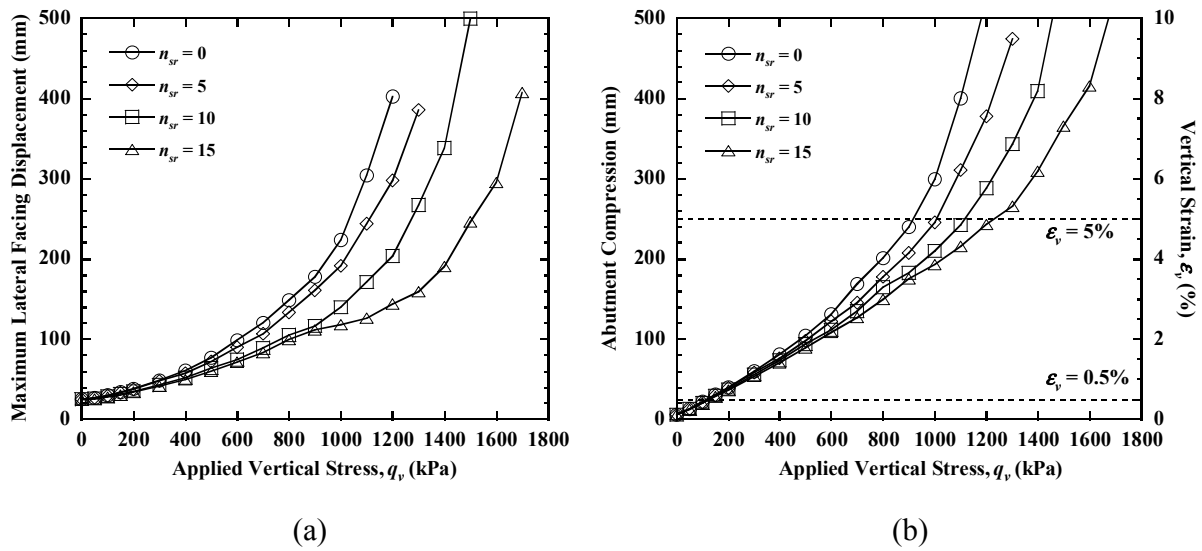


Fig. 10. Effect of secondary reinforcement: (a) maximum lateral facing displacement; (b) abutment compression and vertical strain.

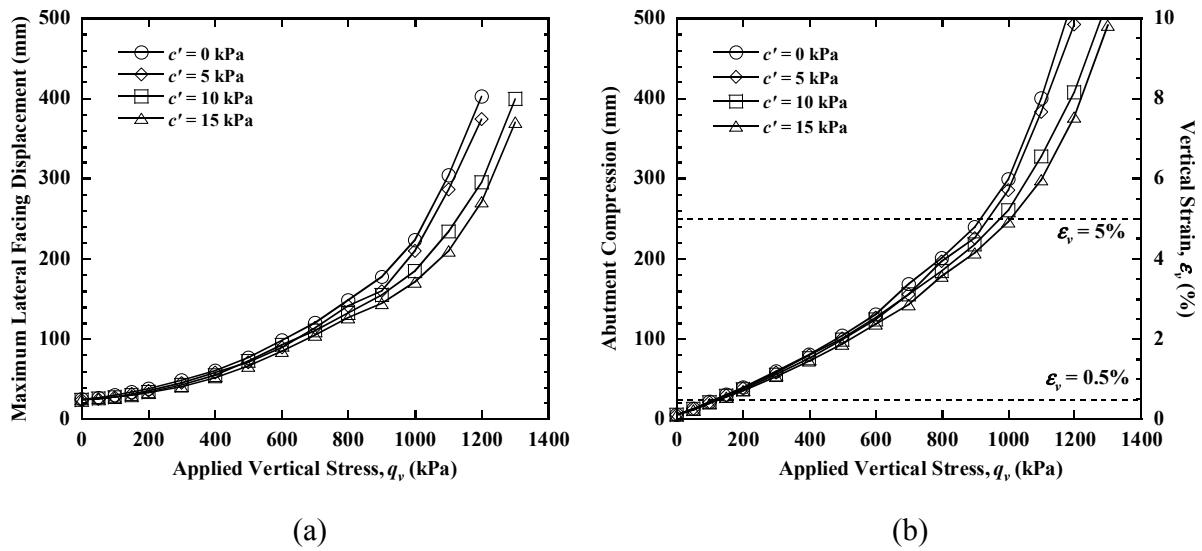


Fig. 11. Effect of backfill soil cohesion: (a) maximum lateral facing displacement; (b) abutment compression and vertical strain.

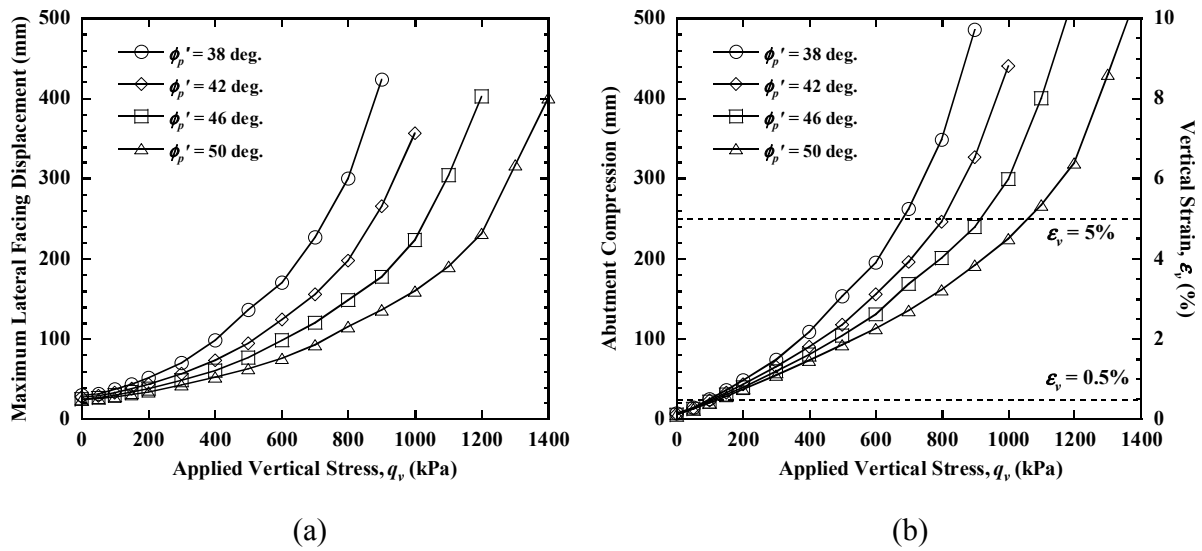


Fig. 12. Effect of backfill soil friction angle: (a) maximum lateral facing displacement; (b) abutment compression and vertical strain.

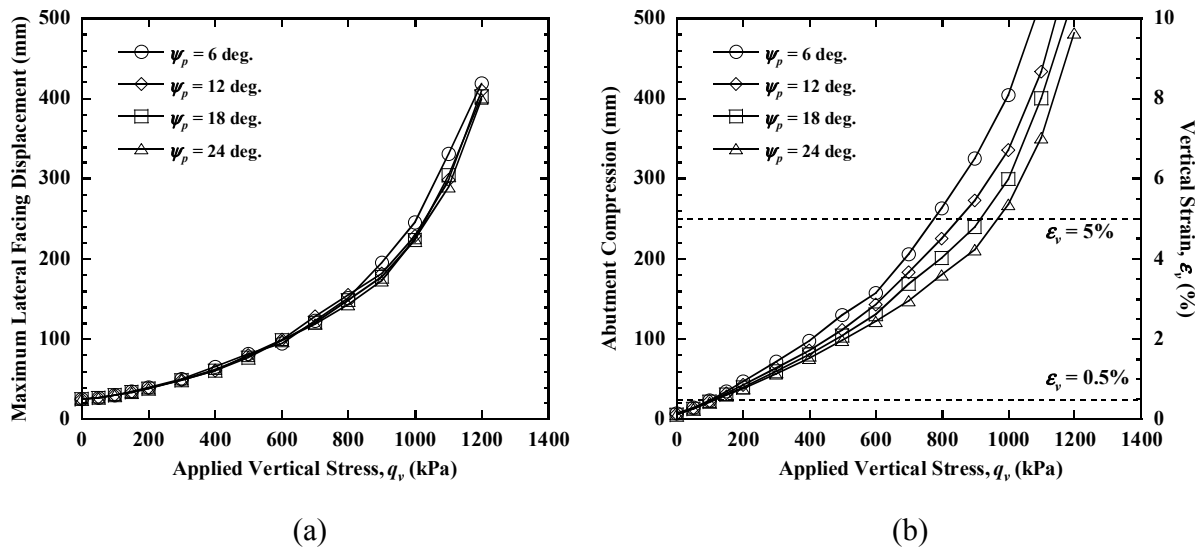


Fig. 13. Effect of backfill soil dilation angle: (a) maximum lateral facing displacement; (b) abutment compression and vertical strain.

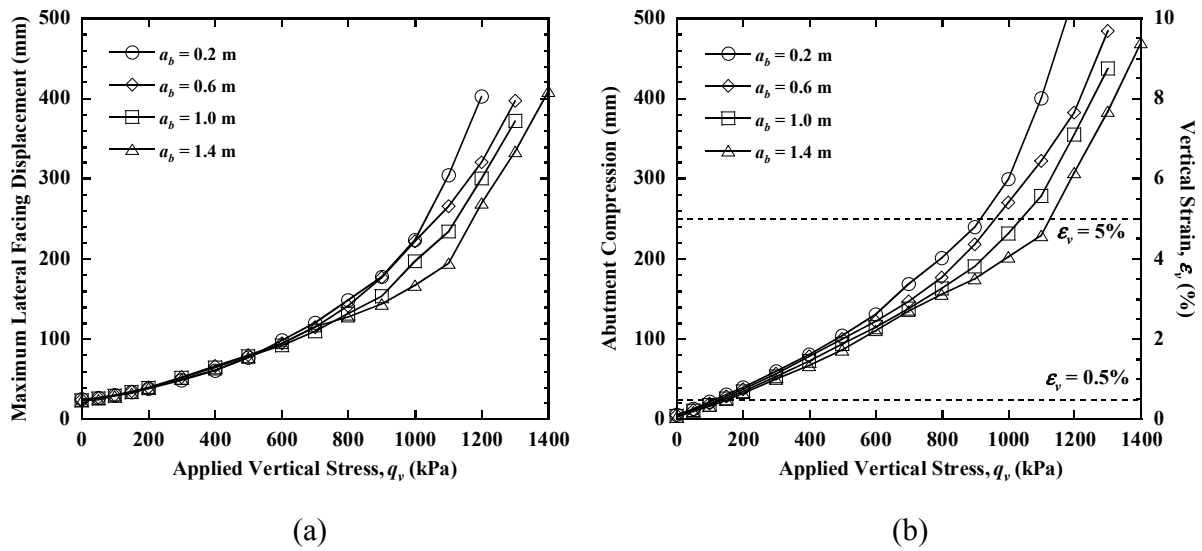


Fig. 14. Effect of bridge seat setback distance: (a) maximum lateral facing displacement; (b) abutment compression and vertical strain.

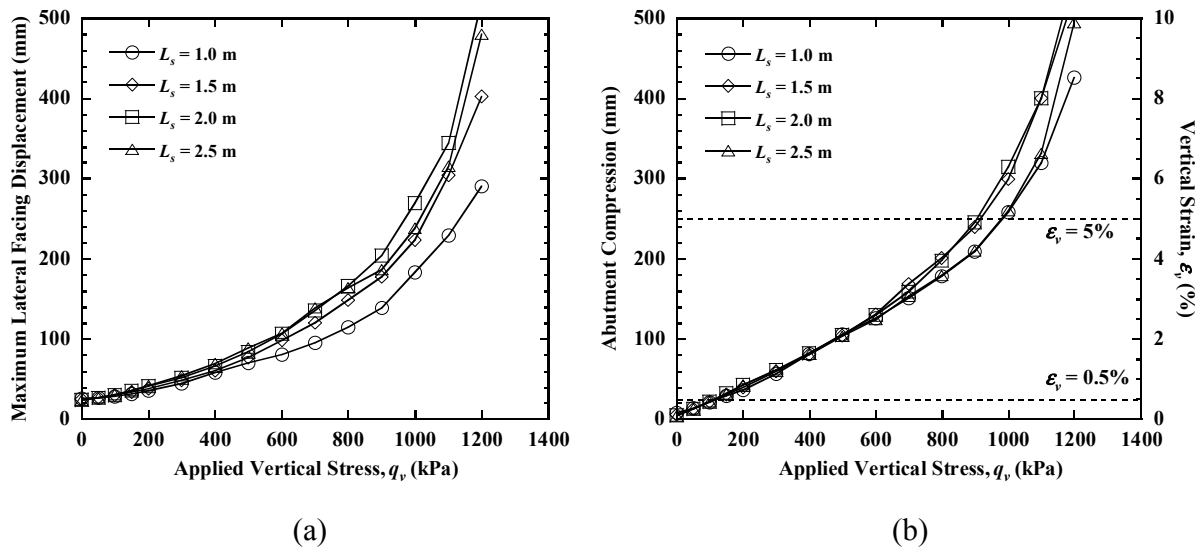


Fig. 15. Effect of bridge seat length: (a) maximum lateral facing displacement; (b) abutment compression and vertical strain.

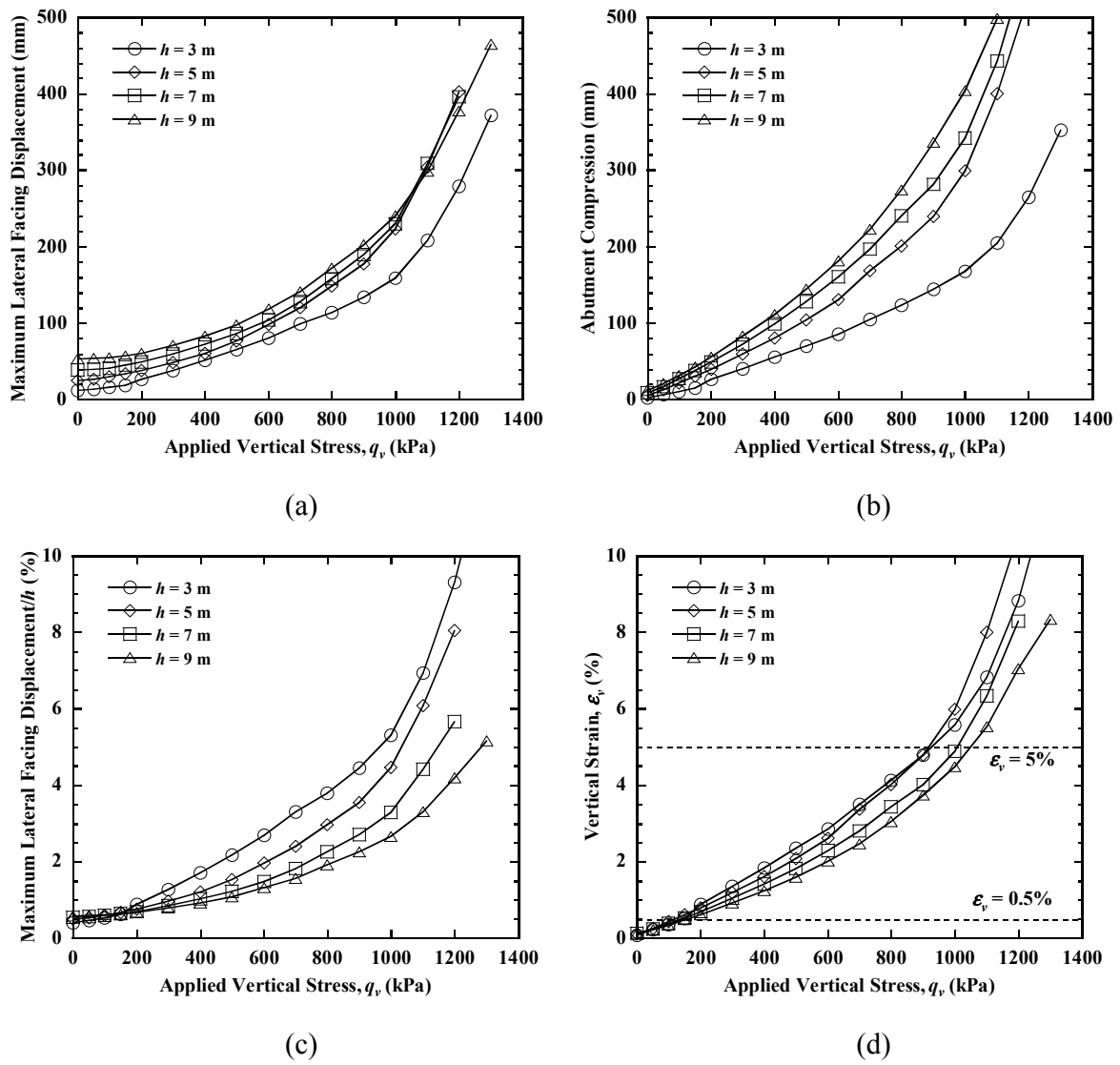


Fig. 16. Effect of abutment height: (a) maximum lateral facing displacement; (b) abutment compression; (c) normalized maximum lateral facing displacement; (d) vertical strain.

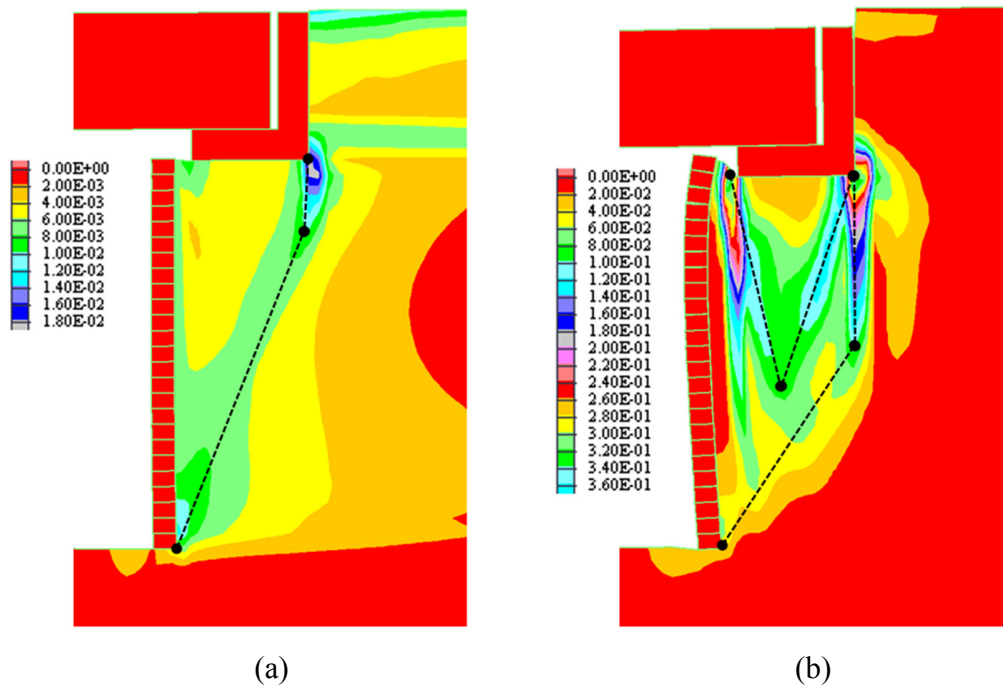


Fig. 17. Contours of shear strain magnitude for baseline case: (a) service limit ($\varepsilon_v = 0.5\%$); (b) strength limit ($\varepsilon_v = 5\%$).

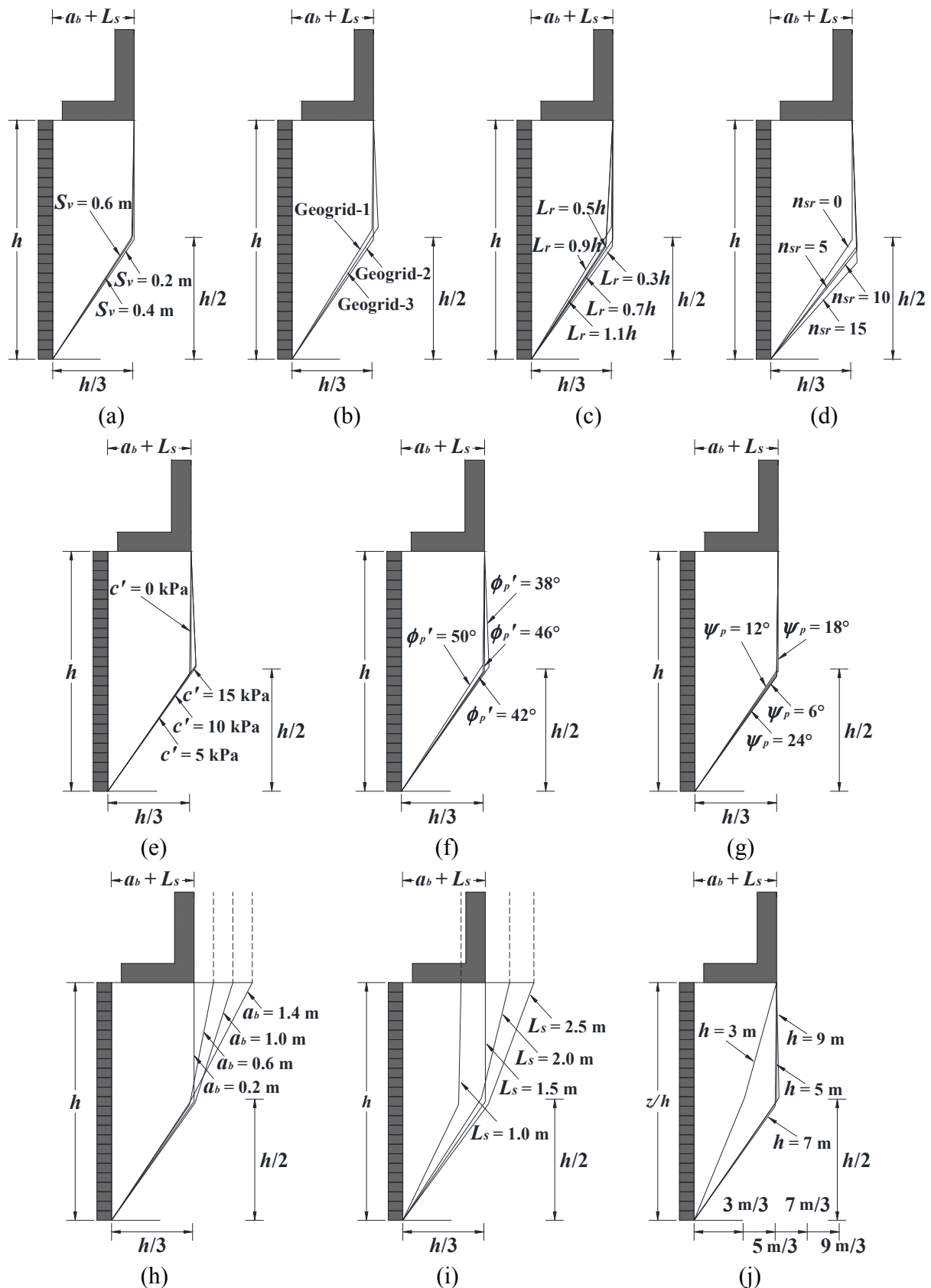


Fig. 18. Bilinear failure surfaces for parametric study: (a) reinforcement spacing; (b) reinforcement stiffness; (c) reinforcement length; (d) secondary reinforcement; (e) backfill soil cohesion; (f) backfill soil friction angle; (g) backfill soil dilation angle; (h) bridge seat setback distance; (i) bridge seat length; (j) abutment height.

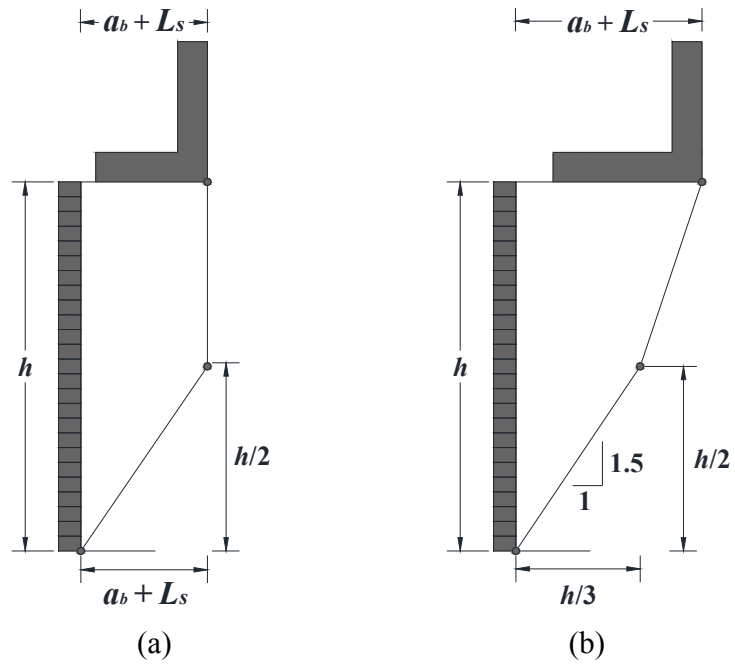


Fig. 19. Proposed general bilinear failure surface for GRS bridge abutments: (a) $a_b + L_s \leq h/3$;

(b) $a_b + L_s > h/3$.

List of Figure Captions

- Fig. 1.** Finite difference grid and boundary conditions for GRS bridge abutment baseline case.
- Fig. 2.** Relationships for soil parameters with incremental plastic shear strain: (a) friction angle; (b) dilation angle.
- Fig. 3.** Comparison of measured and simulated triaxial test results: (a) deviator stress vs. axial strain; (b) volumetric strain vs. axial strain.
- Fig. 4.** Tensile behavior for three HDPE geogrids at $t = 3600$ hours: (a) tensile force-strain relationship; (b) tangent stiffness (parameters from Yu et al. 2016).
- Fig. 5.** Simulation results for $q_v = 400$ kPa and $q_v = 800$ kPa: (a) lateral facing displacement; (b) maximum tensile force in reinforcement.
- Fig. 6.** Simulation results: (a) maximum lateral facing displacement; (b) abutment compression and vertical strain.
- Fig. 7.** Effect of reinforcement spacing: (a) maximum lateral facing displacement; (b) abutment compression and vertical strain.
- Fig. 8.** Effect of reinforcement stiffness: (a) maximum lateral facing displacement; (b) abutment compression and vertical strain.
- Fig. 9.** Effect of reinforcement length: (a) maximum lateral facing displacement; (b) abutment compression and vertical strain.
- Fig. 10.** Effect of secondary reinforcement: (a) maximum lateral facing displacement; (b) abutment compression and vertical strain.
- Fig. 11.** Effect of backfill soil cohesion: (a) maximum lateral facing displacement; (b) abutment compression and vertical strain.
- Fig. 12.** Effect of backfill soil friction angle: (a) maximum lateral facing displacement; (b) abutment compression and vertical strain.
- Fig. 13.** Effect of backfill soil dilation angle: (a) maximum lateral facing displacement; (b) abutment compression and vertical strain.
- Fig. 14.** Effect of bridge seat setback distance: (a) maximum lateral facing displacement; (b) abutment compression and vertical strain.
- Fig. 15.** Effect of bridge seat length: (a) maximum lateral facing displacement; (b) abutment compression and vertical strain.
- Fig. 16.** Effect of abutment height: (a) maximum lateral facing displacement; (b) abutment compression; (c) normalized maximum lateral facing displacement; (d) vertical strain.
- Fig. 17.** Contours of shear strain magnitude for baseline case: (a) service limit ($\varepsilon_v = 0.5\%$); (b) strength limit ($\varepsilon_v = 5\%$).
- Fig. 18.** Bilinear failure surfaces for parametric study: (a) reinforcement spacing; (b) reinforcement stiffness; (c) reinforcement length; (d) secondary reinforcement; (e) backfill soil cohesion; (f) backfill soil friction angle; (g) backfill soil dilation angle; (h) bridge seat setback distance; (i) bridge seat length; (j) abutment height.
- Fig. 19.** Proposed general bilinear failure surface for GRS bridge abutments: (a) $a_b + L_s \leq h/3$; (b) $a_b + L_s > h/3$.